FY20 BISON BWR Fuel Modeling Capability: Material Models

Technical Report

Aysenur Toptan[1] and Kyle Gamble[1]

[1]Idaho National Laboratory

Changing the World's Energy Future

INL
Idaho National
Laboratory

FY20 BISON BWR Fuel Modeling Capability: Material Models

Technical Report

Aysenur Toptan[1] and Kyle Gamble[1]

[1]Idaho National Laboratory

30 September 2020

Idaho National Laboratory
Computational Mechanics and Materials Department
Idaho Falls, Idaho 83415

http://www.inl.gov

Page intentionally left blank

Abstract

Until this year, the BISON fuel performance code has been developed primarily for pressurized water reactor (PWR), accident tolerant fuel (ATF), and advanced reactor (e.g., tri-structural isotropic (TRISO), metallic) analyses. The main focus of this work is to develop and document required material models that would aid predicting cladding failure with a specific hydride distribution to be investigated for boiling water reactor (BWR) applications in the next fiscal year. In terms of materials, the primary differences between a BWR and PWR is the use of gadolinia doping of the UO_2 fuel, the use of Zircaloy-2 for the cladding, and the addition of a liner on the inner surface of the cladding for improved pellet-clad mechanical interaction (PCMI) performance. The liner is typically made of pure zirconium or a lower tin content zirconium alloy (e.g. Zr-0.3%Sn). This work details the development and documentation of material and behavioral models for BWR analysis such as the addition of material and behavior models for gadolinia doped UO_2, pure zirconium, Zr-0.3%Sn, and Zircaloy-2 as well as the ease-of-use additions to allow internal meshing capabilities to include liners. Another important aspect affecting cladding performance is hydrogen diffusion and hydride precipitation in the cladding. A model was added previously for non-lined, homogeneous claddings. In this work, instructions are provided on how to apply the model the BWR liner cladding. Representative experimental values are provided for the hydrogen diffusion parameters and precipitation-dissolution kinetics for typical liner materials of interest.

Page intentionally left blank

Acknowledgments

Page intentionally left blank

Contents

List of Figures

List of Tables

Listings

List of Symbols

Greek Letters

α	Thermal diffusivity $(= k/\rho c_P)$	$\mathrm{m^2/s}$
ν	Poisson's ratio	
θ	Volume fraction of hydrogen in the α-phase	

Roman Letters

A	Area	$\mathrm{m^2}$
Bu	Burnup	MWd/kgU
C	Concentration	wt ppm
c_P	Specific heat capacity	J/kg/K
D_0	Diffusion frequency factor	$\mathrm{m^2/s}$
E	Young's modulus	Pa
E_D	Activation energy	J/mol
E_G	Activation energy for reaction-driven growth	J/mol
f_{clamp}	Factor limiting the maximum hydride content in a node	
G	Shear modulus	Pa
Gd	Gadolinia content	$-$/wt %
k	Thermal conductivity	W/m/K
K_{D0}	Coefficient for dissolution kinetics	$\mathrm{s^{-1}}$
K_{dif0}	Coefficient for diffusion-driven growth kinetics	$\mathrm{s^{-1}}$
K_{Nh0}	Coefficient for nucleation kinetics	$\mathrm{s^{-1}}$
K_{th0}	Coefficient for reaction-driven growth kinetics	$\mathrm{s^{-1}}$
$Q^\star$	Heat of transport	J/mol
Q_D	Activation energy for the solubility	J/mol
Q_P	Activation energy for the super-solubility	J/mol
R	Universal gas constant (=8.3143)	J/mol/K
T	Temperature	K
TSS_{D0}	Coefficient/frequency factor for the solubility	J/mol
TSS_{P0}	Coefficient/frequency factor for the super-solubility	J/mol

Subscripts

∞	Ambient condition
$prec$	Precipitated hydrogen as hydrides
ss	Dissolved hydrogen in the solid solution
95	At 95% theoretical density
el	Electronic
eol	End of life
ph	Phonon–phonon interaction
$self$	Self-irradiation

Acronyms

ALHR	average linear heat rate
ATF	accident tolerant fuel
BWR	boiling water reactor
CASL	Consortium for Advanced Simulation of Light Water Reactors
DOE	U.S. Department of Energy
EOL	end of life
FE	finite element
FGR	fission gas release
HBS	high burnup structure
HBWR	Halden Boiling Water Reactor
HNGD	Hydride Nucleation - Growth - Dissolution Model
IFE	Institutt for Energiteknikk
INL	Idaho National Laboratory
LHR	linear heat rate
LWR	light water reactor
MOOSE	Multiphysics Object-Oriented Simulation Environment
PCMI	pellet-clad mechanical interaction
PWR	pressurized water reactor
RIA	reactivity insertion accident
SQA	software quality assurance
TC	thermocouple
TD	theoretical density
TRISO	tri-structural isotropic
VERA	Virtual Environment for Reactor Applications

Page intentionally left blank

1. Introduction

In 2010, the U.S. Department of Energy (DOE) created its first Energy Innovation Hub, which is focused on developing high-fidelity and high-resolution modeling and simulation tools for the modeling of light water reactors (LWRs). This hub, the Consortium for Advanced Simulation of Light Water Reactors (CASL)[1], has developed an LWR simulation tool called the Virtual Environment for Reactor Applications (VERA). BISON is the high-fidelity and high-resolution fuel performance tool used in VERA.

BISON [1, 2, 3] is a fuel performance code that models the thermo-mechanical behavior of nuclear fuel using high performance modeling and simulation. BISON is established on the Multiphysics Object-Oriented Simulation Environment (MOOSE) framework[2] [4, 5] of Idaho National Laboratory (INL). BISON solves the fully-coupled equations of energy conservation, mechanics, and species conservation to account for a large range of different fuel behavior. It is capable of modeling traditional LWR fuel rods, fuel plates, and tri-structural isotropic (TRISO) fuel particles [6, 7]. It can employ three-dimensional Cartesian, two-dimensional axisymmetric, two-dimensional generalized plane strain, layered two-dimensional, layered one-dimensional, one-dimensional radial spherical geometries. It includes empirical models for a large variety of fuel thermal and mechanical physics.

BWR fuel differs from PWR fuel in terms several aspects, considering (a) extensive use of gadolinia up to 10 wt.%, which significantly impacts the fuel thermal conductivity, consequentially on the fuel temperature distribution; and (b) the use of different alloying materials such as the fuel liners (e.g., pure zirconium or zirconium tin), to increase the margin to PCMI failure, enabling more flexible operation. Such liners tend to exhibit much higher hydrogen contents than the rest of the cladding (in the hottest side of the cladding wall). The concentration of hydrogen and consequent localized precipitation of hydrides can cause the failure of the cladding at small strains.

This study focuses on expanding BISON's BWR fuel modeling capability by developing needed material models that would aid in predicting cladding failure with a specific hydride distribution, taking into account the hydride geometry and hydrogen distribution within the liner cladding. As a part of the work scope, Fiscal Year 2020 (FY2020) focused on the addition of materials modeling to allow the use of different alloying materials and gadolinia up to 10 wt.%. The tasks to be completed in FY2020 are: (1) to complete an initial assessment of material model needs for BWR fuel, which is completed prior to this milestone report; and

---

[1]www.casl.gov

[2]a high-performance, open source, C++ FE framework: `www.github.com/idaholab/moose`

(2) to develop and document material models for BWR fuel in BISON including verification and validation, which is the scope of this milestone report.

This report is organized as follows: Chapter 2 describes BISON's modeling options of the *Gd*-bearing UO_2 thermal properties as well as the liner materials, such as pure zirconium, zirconium tin, and Zircaloy-2 thermal and/or mechanical properties in addition to the behavioral model for the hydrogen migration and redistribution within a Zircaloy cladding. Chapter 3 outlines BISON's internal meshing capabilities for the liner layer being added to the inner face of cladding. Chapter 4 covers the validation activities in which BISON's predictions are compared to the measurements from Halden IFA-681.1 experiment. Chapter 5 concludes the document with a discussion of the results and future work. Lastly, the publication documenting BISON's new thermal conductivity capability for gadolinia-bearing uranium dioxide fuel prior to the addition of the latest models described within this report are highlighted in Chapter 6.

2. Materials/Behavioral Models

In this chapter, the material property models of BISON for BWR fuel rod analysis are documented, which are tabulated in Table 2.1. The materials of interest are uranium dioxide fuel with gadolinia, Gd_2O_3, addition (see Section 2.1) and liner cladding material models, such as pure zirconium (see Section 2.2), zirconium tin (see Section 2.3), and/or Zircaloy-2 properties (see Section 2.4). Lastly, the new features are being documented, integrated into the BISON test suite, and run periodically to ensure that code capabilities are not lost. It should be noted that models for low tin content alloys, as with pure zirconium for nuclear applications, are scarce in the open literature. In absence of a specific model for liners, Zircaloy-2 properties can be used. All of the Zircaloy-2 models presented in this chapter are existing models of BISON and are provided for the purposes of completeness. Additional properties for UO_2-Gd_2O_3 fuels are not presented here, owing to the absence properties in the literature; the assumption is to use the same material models as those used for UO_2 without the gadolinia addition. Lastly, an important physics (a so-called behavioral model) to consider for BWR fuel rod behavior is the hydrogen migration and redistribution model, which is briefly outlined in Section 2.5.

Table 2.1. Material models available for BWR analyses.

Property	Description	BISON source code
UO_2-Gd_2O_3 properties		
2.1	thermal conductivity up to 60MWd/kgU	ThermalFuel
2.2	thermal conductivity at extended burnup	ThermalFuel
2.3	specific heat capacity	ThermalFuel
Pure zirconium properties		
2.4	thermal conductivity	ZrThermal
2.5	specific heat capacity	ZrThermal
2.6	thermal expansion eigenstrain	ZrThermalExpansionEigenstrain
Zirconium tin properties		
2.7	thermal creep	ZrSnCreepUpdate
Zircaloy-2 properties		
2.8	thermal conductivity	ThermalZry
2.9	specific heat capacity	ThermalZry
2.10	elastic properties	ZryElasticityTensor
2.11	thermal expansion	ZryThermalExpansionEigenstrain
2.12	thermal and irradiation creep	ZryCreepLOCAErbacherLimbackHoppeUpdate
2.13	irradiation growth	ZryIrradiationGrowthEigenstrain

2.1 UO$_2$–Gd$_2$O$_3$ Properties

Thermal Properties

This section covers newly implemented/updated thermal modeling options in BISON under three main categories: Property 2.1 for thermal conductivity models that are valid up to 60MWd/kgU; Property 2.2 for thermal conductivity models at extended burnups; and Property 2.3 for the specific heat capacity.

Property 2.1: UO$_2$-Gd$_2$O$_3$ fuel, thermal conductivity up to 60MWd/kgU (`ThermalFuel`)

A new thermal conductivity model is developed using an extensive set of experimental data [8], referred to as the `Toptan` model in the code. The model form is expressed in terms of T is the fuel temperature (°C), Gd is the fraction of the gadolinia content (weight fraction), and Bu is the burnup (MWd/kgU), which is given by

$$k_{95} = k_{ph} + k_{el} \tag{2.1a}$$

$$k_{ph} = \frac{1}{0.1149 + 2.2748 \times 10^{-4}T + 1.2027gd + 2.3655 \times 10^{-3}Bu + \frac{6.7927 \times 10^{-3}Bu^{0.28}(1 - 0.9\exp(-0.04Bu))}{1 + 396\exp\left(-\frac{6380}{T}\right)}}, \tag{2.1b}$$

$$k_{el} = 7.5620 \times 10^{-3}\exp\left(2.0081 \times 10^{-3}T\right), \tag{2.1c}$$

The thermal conductivity normalized to a given porosity p (unitless) [9] is obtained by

$$k = k_{100}\left(\frac{1.0 - p}{1.0 + \beta p}\right), \tag{2.2}$$

where k_{100} is the thermal conductivity of the non-porous material, and $\beta(=0.5)$ is the geometrical factor [10]. Eq. 2.2 can be applied to k_{95} by simply inserting $k_{100} = 1.07895k_{95}$ into the above relation. Existing literature thermal conductivity models that account for the gadolinia addition are tabulated in Table 2.2. These models exist in BISON prior to this project. A detailed review of this modeling was performed to confirm that they are implemented in the code properly.

Property 2.2: UO$_2$-Gd$_2$O$_3$ fuel, thermal conductivity at extended burnup (`ThermalFuel`)

The thermal conductivity, k (W/m/K) at 95% theoretical density (TD) (i.e., normalized to 5 vol.% as-fabricated porosity) is given by [11, 12] in the following form:

$$k_{95} = \frac{1}{A(T_{irr}, T_{ann}, bu) + B(T_{irr}, T_{ann}, bu)T} \tag{2.3}$$

where bu is the burnup (GWd/t), T_{irr} is the irradiation temperature (K), T_{ann} is the maximum temperature reached during out-of-pile annealing (K), and T is the instant application temperature

(K). A and B are the empirical coefficients which are formulated as follows:

- **Coefficient $A(T_{irr}, T_{ann}, bu)$.** [11] defines the coefficient A as:

$$A(T_{irr}, T_{ann}, bu) = \delta A + \Gamma(bu, GIS) + 0.046 \tag{2.4}$$

Note that [12] replaces 0.046 with 0.092623 for non-doped fuel ($gd = 0$) and $0.0524 + 0.3079 \times 10^{-2}gd + 12.2031 \times 10^{-4}gd^2$ for the non-zero gadolinia additive, where gd is the gadolinia content in wt.%.

The effect of the irradiation defects on A is defined in terms of the out-pile self-irradiation effect, δA_{Self} and the effective concentration of irradiation defects at end of life (EOL), δA_{EOL} as

$$\delta A = \delta A_{Self}(T_m, bu) + \delta A_{EOL}(T_m, bu) \tag{2.5}$$

where T_m is the maximum temperature of T_{irr} and T_{ann} (i.e., $T_m = \max(T_{irr}, T_{ann})$).

$$\delta A_{Self}(T_m, bu) = \begin{cases} 0.02F(bu) & \text{if } T_m \le 900K \\ 0.02F(bu)\frac{1450-T_m}{1450-900} & \text{if } 1450K > T_m > 900K \\ 0 & \text{if } T_m \ge 1450K. \end{cases} \tag{2.6}$$

$$\delta A_{EOL}(T_m, bu) = \frac{bu}{850}\left[\frac{1}{1 + \exp\left(\frac{T_m - 950}{25}\right)} + \frac{1}{1 + \exp\left(\frac{T_m - 1300}{35}\right)} - 0.0525\right] \tag{2.7}$$

$$F(bu) = \frac{1}{1 + \exp\left(\frac{20-bu}{6}\right)} - 0.015267 \tag{2.8}$$

In [12], 0.015267 is replaced with 0.03444 in their formulation.

The contribution of nonvolatile and volatile fission products is incorporated to the thermal conductivity model by [11, 12] as:

$$\Gamma(bu, GIS) = 9.02 \times 10^{-4}buGIS + 1.74 \times 10^{-3}bu + 7.51 \times 10^{-3} \tag{2.9}$$

where GIS is the fraction of volatile fission products present as dispersed atoms in the fuel matrix and is expressed by

$$GIS = \frac{1 - 0.9IRIM}{\left[1 + \exp\left(\frac{T_{irr}-1350}{200}\right)\right]\left[1 + \exp\left(\frac{T_{ann}-1350}{200}\right)\right]} \tag{2.10}$$

in terms of

$$IRIM = \frac{1}{\left[1 + \exp\left(\frac{T_{irr}-950}{30}\right)\right]\left[1 + \exp\left(\frac{73-bu}{2}\right)\right]}. \tag{2.11}$$

- **Coefficient** $B(T_{irr}, T_{ann}, bu)$. [11] defines the coefficient B as:

$$B(T_{irr}, T_{ann}, bu) = B_0 + (B_1 - B_0) \left(1 - \frac{\delta B}{6.5 \times 10^{-5}}\right) \tag{2.12}$$

$$B_0 = -1.65 \times 10^{-6} bu + 2.55 \times 10^{-4} - 3.6 \times 10^{-5} IRIM \tag{2.13}$$

$$B_1 = 4.2 \times 10^{-7} bu + 2.75 \times 10^{-4} \tag{2.14}$$

In [12], 2.75×10^{-4} is replaced with 2.217×10^{-4} for non-doped fuel ($Gd = 0$) and, for a non-zero gadolinia additive, 2.75×10^{-4} is replaced with $2.553 \times 10^{-4} + 8.606 \times 10^{-6} gd - 0.0154 \times 10^{-4} gd^2$ where gd is the gadolinia content in wt.%.

$$\delta B = F(bu) \delta B_{EOL}(T_m, bu) \tag{2.15}$$

$$\delta B_{EOL}(T_m, bu) = \frac{bu}{34} \left[\frac{4.0 \times 10^{-5}}{1 + \exp\left(\frac{T_m - 950}{25}\right)} + \frac{2.5 \times 10^{-5}}{1 + \exp\left(\frac{T_m - 1300}{35}\right)} \right] \tag{2.16}$$

To ensure that the model (2.2) is implemented in BISON correctly and outputs in reasonable values, we create the thermal conductivity plots. Fig. 2.1 shows the model comparison from each model at various temperatures. The models differentiate from each other slightly for the non-doped uranium dioxide fuel.
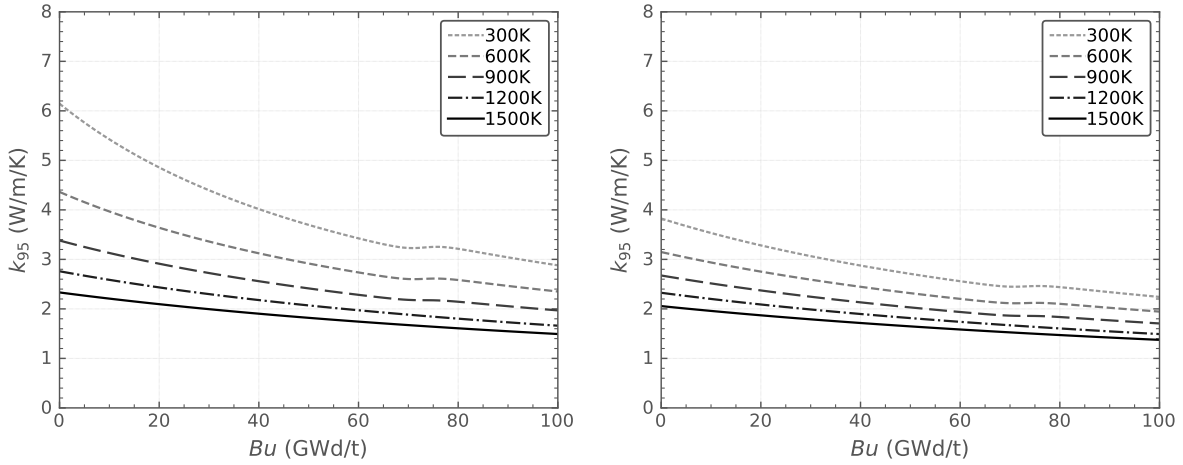
(a) The Staicu model ($Gd = 0$).

(b) The Staicu model ($Gd = 10 \, \text{wt} \, \%$).

Figure 2.1. Comparison of the thermal conductivity model at $T = T_{irr}$ using (a) the Ronchi model, (b) the Staicu model, and (c) the Staicu model with an arbitrary gadolinia concentration of 10wt.%. The thermal conductivity increases in the transition region where the HBS commences to form. [13] attributes the increase in the thermal conductivity in the HBS formation to the decrease in the fission gas concentration dissolved in the matrix. The degradation of the thermal conductivity resumes as a result of the accumulation of fission products for further increase of the burnup.

Table 2.2. A list of the conventional Gd-doped UO_2 thermal conductivity models in BISON. The formulation of each model is provided along with the reported applicability range. Maxwell's relation (Eq. 2.2) is applied for the porosity correction unless it is reported differently. The units of the state variables: k(W/m-K), T_K(K), T_C(°C), p(–), Bu(MWd/kgU), B(MWd/kg urania), β(at.%), and gd(weight fraction).

Formulation	Applicability
The Halden model [14, p.3.4]	
$k_{95} = k_{ph} + k_{el}$ $k_{ph} = \frac{1}{0.1148+1.1599(gd+x)+0.0040B+2.475\times10^{-4}(1-0.00333B)\min(1650,T_c)}$ $k_{el} = 0.0132\exp\left(0.00188 T_c\right)$	T in $[300\,\text{K},3000\,\text{K}]$ Bu in $[0,62\,\text{GWd/MTU}]$ Pu in $[0,7\,\text{wt}\,\%]$ TD in $[92\,\%,97\,\%]$
The modified NFI model [14]	
$k_{95} = k_{ph} + k_{el}$, $k_{ph} = \frac{1}{0.0452+1.1599gd+2.46\times10^{-4}T+0.00187Bu+\frac{0.038Bu^{0.28}[1-0.9\exp\left(-0.04Bu\right)]}{(1+396\exp\left(-6380/T\right))}}$, $k_{el} = \frac{3.5\times10^9}{T^2}\exp(-\frac{16361}{T})$	T in $[300\,\text{K},3000\,\text{K}]$ Bu in $[0,62\,\text{GWd/MTU}]$ TD in $[92\,\%,97\,\%]$ Gd in $[0,10\,\text{wt}\,\%]$
The NFIR model [15, 16]	
$k_{95} = (1-F)k_{start} + Fk_{end} + k_{el}$ $F = 0.5\left(1 + \tanh\left(\frac{T_c-900}{150}\right)\right)$, $k_{start} = \frac{1}{term_0+6.14\times10^{-3}Bu-1.4\times10^{-5}Bu^2+\{2.5\times10^{-4}\exp\left(-1.268763gd\right)-1.81\times10^{-6}Bu\}T_c}$, $k_{end} = \frac{1}{term_0+2.6\times10^{-3}Bu+\{2.5\times10^{-4}\exp\left(-1.268763gd\right)-2.7\times10^{-7}Bu\}T_c}$ $k_{el} = 0.0132\exp\left(0.00188 T_c\right)$, $term_0 = \begin{cases} 9.592\times10^{-2}, & gd = 0 \\ gdir\cdot gdfac, & gd \neq 0 \end{cases}$ $gdir = 0.1197\tanh\left(1\times10^2 gd\right)^{0.1} + 1.214167gd + 5.40625gd^2 - 51.82292gd^3$ $gdfac = 0.65227273 + 2.7273gd - 2.25gd\tanh\left(1\times10^{-5}Bu\right)$ The porosity correction multiplier is: $\left(\frac{1.0-p[2.58-5.8\times10^{-4}T_C]}{1.0-0.05[2.58-5.8\times10^{-4}T_C]}\right)$	

Property 2.3: UO₂-Gd₂O₃ fuel, specific heat capacity (`ThermalFuel`)

The specific heat capacity (J/kg/K) is expressed by:

$$c_P = \frac{K_1 \theta^2 \exp\left(\frac{\theta}{T}\right)}{T^2 \left[\exp\left(\frac{\theta}{T}\right) - 1\right]^2} + K_2 T + \frac{Y K_3 E_D}{2RT^2} \exp\left(-\frac{E_D}{RT}\right) \tag{2.17}$$

where T is the temperature (K), Y is the oxygen-to-metal ratio (-), and R is the universal gas constant (8.3143 J/mol/K). The empirical coefficients (K_1, K_2, K_3, θ, and E_D) are tabulated in Table 2.3 for UO₂ and GdO₂. The specific heat capacity of Gd-doped UO₂ fuels (see Fig. 2.2) is computed as:

$$c_P = (1 - Gd)c_{P,UO_2} + Gd c_{P,GdO_2} \tag{2.18}$$

in terms of the fraction of gadolina content, Gd (-), and the specific heat capacity, $c_{P,i}$ for $i =$ UO₂ and GdO₂.

Table 2.3. The empirical constants used in Eq. 2.17 from [17].

	K_1 (J/kg/K)	K_2 (J/kg/K²)	K_3 (J/kg)	θ (K)	E_D (J/mol)
UO₂	296.70	2.430×10⁻²	8.745×10⁷	535.285	1.577×10⁵
GdO₂	315.86	4.044×10⁻²	0.0	348.000	0.0
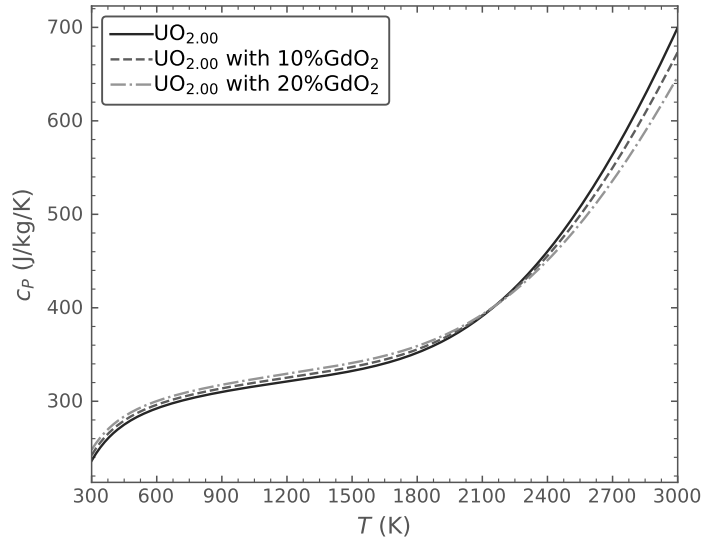
Figure 2.2. Specific heat capacity of UO₂ at arbitrarily chosen gadolinia concentrations (0 to 20 wt.%).

2.2 Pure Zirconium Properties

Pure zirconium is one material used for liners in BWRs. For nuclear applications, the majority material property correlations are for the zirconium alloys Zircaloy-2 and Zircaloy-4. In BWRs, the cladding material is Zircaloy-2; thus, for material properties for which a pure zirconium model is unavailable, those of Zircaloy-2 (see Section 2.4) are used.

Thermal Properties

Property 2.4: Pure zirconium, thermal conductivity (`ZrThermal`)

The thermal conductivity (W/m-K) of pure zirconium is given by [18]:

$$k = 8.8527 + 7.0820 \times 10^{-3}T + 2.5329 \times 10^{-6}T^2 + \frac{2.9918 \times 10^3}{T} \tag{2.19}$$

where T is the temperature (in K) and is valid in $[298\,\text{K}, 2000\,\text{K}]$.

Property 2.5: Pure zirconium, specific heat capacity (`ZrThermal`)

The specific heat correlation depends upon whether the zirconium is in the α-phase ($298 \leq \text{T} \leq 1139$ K) or β-phase ($1139 < \text{T} \leq 2128$ K) [18].

$$c_P = \begin{cases} 24.1618 + 8.75582 \times 10^{-3}T - \frac{69942}{T^2} & \alpha\text{-phase} \\ 25.607406 + 6.80168 \times 10^{-4}T + 5.837384 \times 10^{-8}T^2 + 9.13714728 \times 10^{-10}T^3 - \frac{50466}{T^2} & \beta\text{-phase} \end{cases} \tag{2.20}$$

where T is the temperature (in K).

Mechanical Properties

Property 2.6: Pure zirconium, thermal expansion (`ZrThermalExpansionEigenstrain`)

This material calculates the temperature dependent thermal expansion of Zr using a correlation from [18]. The thermal expansion ($\Delta L/L$) is written in terms of temperature, T (in K):

$$\frac{\Delta L}{L} = \begin{cases} -1.11 \times 10^{-3} + 2.325 \times 10^{-6}T + 5.595 \times 10^{-9}T^2 - 1.768 \times 10^{-12}T^3 & \alpha\text{-phase} \\ -7.59 \times 10^3 + 1.474 \times 10^{-6}T - 5.140 \times 10^{-9}T^2 + 1.559 \times 10^{-12}T^3 & \beta\text{-phase} \end{cases} \tag{2.21}$$

2.3 Zirconium Tin Properties

Low tin content ($<1\%$) zirconium-tin alloys are another option used for BWR liners. As with pure zirconium, models for low tin content alloys for nuclear applications is scarce; therefore, in the absence of a specific model, those of Zircaloy-2 (see Section 2.4) are used.

Mechanical Properties

Property 2.7: Zirconium tin, thermal creep (`ZrSnCreepUpdate`)

The creep rate is a given by [19]:

$$\dot{\epsilon} = A \left[\sinh\left(\alpha\sigma\right)\right]^n \exp\left(-\frac{Q}{RT}\right) \tag{2.22}$$

where A (s^{-1}), α (MPa^{-1}), n (-), and Q (kJ/mol) are material parameters, R (kJ/mol-K) is the ideal gas constant, and T (K) is the temperature. The material constants are are all fourth order polynomials of the inelastic strain, ϵ, as follows:

$$\ln\left(A\right) = \sum_{i=0}^{4} A_i \epsilon^i, \qquad \alpha = \sum_{i=0}^{4} B_i \epsilon^i, \qquad n = \sum_{i=0}^{4} C_i \epsilon^i, \quad \text{and} \quad Q = \sum_{i=0}^{4} D_i \epsilon^i. \tag{2.23}$$

where A_i through D_i are the coefficients, which are provided in Table 2.4.

Table 2.4. Coefficients used in the polynomial fits for the material constants used in the Zr-0.3%Sn creep correlation.

	$i = 0$	$i = 1$	$i = 2$	$i = 3$	$i = 4$
A_i	53.365	-39.774	-40.405	287.21	-264.92
B_i	0.0347	-0.2091	0.817	-1.3775	0.85420
C_i	3.6433	40.123	-201.32	373.51	-242.19
D_i	506.22	-730.03	1345.3	-466.67	-433.33

2.4 Zircaloy-2 Properties

Zircaloy-2 is the cladding material of choice in BWRs. This section outlines the material models available in BISON for Zircaloy-2. As described in previously, the material models (except irradiation growth) described in this section are also applied to liners when a specific liner material does not exist. The cold work of Zircaloy-2 is taken as 0% [17].

Thermal Properties

Property 2.8: Zircaloy-2, thermal conductivity (`ThermalZry`)

The thermal conductivity is given by

$$k = 7.668 \times 10^{-8}T^3 - 1.450 \times 10^{-5}T^2 + 2.088 \times 10^{-2}T + 7.511 \tag{2.24}$$

where T is the temperature (in K).

Property 2.9: Zircaloy-2, specific heat capacity (`ThermalZry`)

The specific heat is also obtained from MATPRO and is a piecewise linear function of the tabulated values in Table 2.5. For values above $1248\,\text{K}$ the specific heat is set to $356\,\text{J/kg/K}$.

Table 2.5. Specific heat capacities for Zircaloy.

T(K)	c_P(J/kg/K)	T(K)	c_P(J/kg/K)
300	281	1153	719
400	302	1173	816
640	331	1193	770
1090	375	1213	619
1093	502	1233	469
1113	590	1248	356
1133	615		

Mechanical Properties

Property 2.10: Zircaloy-2, elastic constants (ZryElasticityTensor)

The Young's modulus in the α and β phases is calculated by:

$$E = \begin{cases} \dfrac{(1.088 \times 10^{11} - 5.475 \times 10^7 T + (6.61 \times 10^{11} + 5.912 \times 10^8 T)\Delta)}{0.88 + 0.12\exp\left(-\frac{\phi}{1\times10^{25}}\right)} & \alpha\text{-phase} \\ 9.21 \times 10^{10} - 4.05 \times 10^7 T & \beta\text{-phase} \end{cases} \quad (2.25)$$

and the shear modulus is

$$G = \begin{cases} \dfrac{4.04 \times 10^{10} - 2.168 \times 10^7 T + (7.07 \times 10^{11} - 2.315 \times 10^8 T)\Delta}{0.88 + 0.12\exp\left(-\frac{\phi}{1\times10^{25}}\right)} & \alpha\text{-phase} \\ 3.49 \times 10^{10} - 1.66 \times 10^7 T & \beta\text{-phase} \end{cases} \quad (2.26)$$

where T (K) is the temperature, Δ is the average oxygen concentration minus the oxygen concentration of the as-received alloy, and ϕ (n/m^2) is the fast neutron fluence. It should be noted that there is a cold work contribution to the general equations for E and G, which have been ommitted here because the cold work for Zircaloy-2 is 0%. The Poisson's ratio, ν is computed via the following relation:

$$\nu = \frac{E}{2G} - 1 \quad (2.27)$$

Property 2.11: Zircaloy-2, thermal expansion (ZryThermalExpansionEigenstrain)

The thermal expansion of these materials is anisotropic with different strains forming in the diametrical and axial directions. The diametrical and axial thermal strains, ϵ_{dia} and ϵ_{axial}, are given by MATPRO in the α-phase ($T < 1073\,\text{K}$) and β-phase ($T > 1244\,\text{K}$):

$$\epsilon_{axial} = \begin{cases} -2.5060 \times 10^{-5} + 4.441 \times 10^{-6} T_C & \alpha\text{-phase} \\ -8.3 \times 10^{-3} + 9.70 \times 10^{-6} T_C & \beta\text{-phase} \end{cases} \quad (2.28)$$

$$\epsilon_{dia} = \begin{cases} -2.373 \times 10^{-4} + 6.721 \times 10^{-6} T_C & \alpha\text{-phase} \\ -6.8 \times 10^{-3} + 9.70 \times 10^{-6} T_C & \beta\text{-phase} \end{cases} \quad (2.29)$$

The linear interpolation is employed between the α and β-phase values is used in the $\alpha + \beta$-phase ($1073\,\text{K} \leq T \leq 1244\,\text{K}$).

Property 2.12: Zircaloy-2, creep (`ZryCreepLOCAErbacherLimbackHoppeUpdate`)

Low temperature thermal creep of Zircaloy-2 is given by the Limbäck-Andersson [20] model:

$$\dot{\epsilon}_{th\_low} = 5.47 \times 10^8 \frac{E}{T} \left(\sinh \left(\frac{a_i \sigma_{eff}}{E} \right) \right)^3 .5 \exp \left(-\frac{198000}{RT} \right)$$

$$a_i = 650 \left[1.0 - 0.56 \left(1 - e^{(-1.4 \times 10^{-24} \Phi^{1.3})} \right) \right] \tag{2.30}$$

$$E = 1.148 \times 10^5 - 59.9T$$

where $\dot{\epsilon}_{th\_low}$ is the low temperature thermal creep rate (hr^{-1}), E is the Young's modulus (MPa), T is the temperature (K), Phi is the fast neutron fluence (n/cm^2), σ_{eff} is the effective (Von Mises) stress (MPa), and R is the ideal gas constant $(8.314\,\mathrm{J/mol-K})$. High temperature $(> 900\,\mathrm{K})$ thermal creep of the Zircaloy-2 is of the form [21]:

$$\dot{\epsilon}_{th\_high} = A \sigma_{eff}^n \exp \left(-\frac{Q}{RT} \right) \tag{2.31}$$

where $\dot{\epsilon}_{th\_high}$ is the high temperature creep rate (s^{-1}), A is the creep coefficient, σ_{eff} is the effective (Von Mises) stress, n is the stress exponent, and Q is the activation energy. These parameters depend upon the phase of the alloy, as summarized in Table 2.6, where the activation energy in the α-phase is given by:

$$A = 3.21 \times 10^5 + 24.69 \, (T - 923.15) \tag{2.32}$$

Linear interpolation is used for mixed phases not equal to 50%α–50%β for $\epsilon \leq 3 \times 10^{-3}$. For $\epsilon > 3 \times 10^{-3}$ linear interpolation is used for Q and n and linear interpolation of $\ln{(A)}$ is used for A. Between the low temperature creep model upper limit of $> 700\mathrm{K}$ and the lower limit of $> 900\mathrm{K}$ for the high temperature creep model interpolation between the two correlations are used.

The irradiation creep law used for Zircaloy-2 (with a recrystallized annealed microstructure) is given by:

$$\dot{\epsilon}_{irr} = 1.654 \times 10^{-24} \phi^{0.85} \sigma_{eff} \tag{2.33}$$

where $\dot{\epsilon}_{irr}$ is the irradiation creep rate (hr^{-1}), ϕ is the fast neutron flux (n/m^2-s), and σ_{eff} is the effective stress (MPa).

> **Property 2.13: Zircaloy-2, irradiation growth (`ZryIrradiationGrowthEigenstrain`)**
>
> Zircaloy-2 undergoes axial growth and subsequent diametrical shrinkage due to irradiation. The correlation of irradiation growth is given by:
>
> $$\epsilon_{irr} = 1.09 \times 10^{-21} \Phi^{0.845} \tag{2.34}$$
>
> where Φ is the fast neutron fluence (n/m^2).

Table 2.6. Parameters for high temperature creep of Zircaloy-2.

Phase	A(MPa^n/s)	Q (kJ/mol)	n (-)
α	8737	See Eq. 2.32	5.89
50%α–50%β	0.24	1.02355×10^5	2.33
β	7.9	1.41919×10^5	3.78

2.5   Hydrogen Migration/Redistribution Model of BISON

The use of different alloying materials, such as the fuel liners (e.g., pure zirconium or zirconium tin), to increase the margin to PCMI failure, enabling more flexible operation. Such liners tend to exhibit much higher hydrogen contents than the rest of the cladding (in the hottest side of the cladding wall)[1]. The concentration of hydrogen and consequent localized precipitation of hydrides can cause the failure of the cladding at small strains. Our task for this report is to document the BISON's existing model for the hydrogen migration and redistribution in the cladding.

Background   The hydride migration and redistribution is schematically illustrated in Fig. 2.3. Hydrogen is picked/absorbed by the cladding from the chemical reaction occurring at the outer surface of the cladding with the water (i.e., oxidation). Later, hydrogen is transported in the cladding via two main diffusion mechanisms in which driving forces are temperature and concentration gradients that apply in opposite directions: Soret effect and Fickian diffusion, respectively. Depending upon the applied stress, the orientation of hydride precipitation will differentiate.

Previous studies on the hydrogen migration and redistribution in BISON are performed and/or implemented by several researchers [24, 25, 26, 27, 28]. Herein, we provide a brief summary of up-to-date model (available) in the code—referred to as the Hydride Nucleation - Growth - Dissolution Model (HNGD)—is

---

[1]Experimental evidence can be found in the literature, particularly for the liner-cladding geometry in [22, 23].

given by the following formation:

$$\frac{\partial T}{\partial t} = \alpha \nabla^2 T$$

$$\frac{\partial C_{Prec}}{\partial t} = S \qquad (2.35)$$

$$\frac{\partial C_{ss}}{\partial t} = -\nabla \left(-D\nabla C_{ss} - \frac{DQ^\star C_{ss}}{RT^2} \delta T \right) - S$$

where T is temperature, α is thermal diffusivity, C_{prec} is the concentration of precipitated hydrogen as hydrides, C_{ss} is the concentration of dissolved hydrogen in the solid solution, $Q^\star$ is the heat of transport, and R is the universal gas constant ($8.3143\,\text{J/mol/K}$). The diffusion coefficient is computed according to the Arrhenius law: $D = D_0 \exp\left(-E_D/RT\right)$ in terms of D_0 is the constant and E_D is the activation energy.
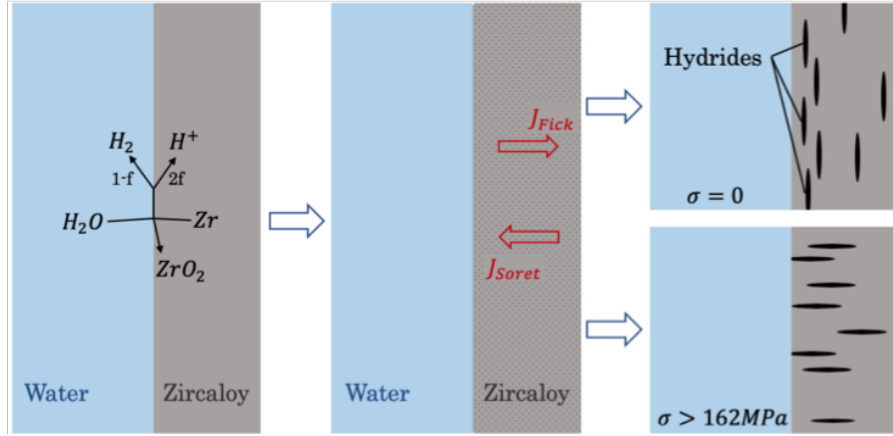
Figure 2.3. Schematic illustration of hydride migration and redistribution within a Zircaloy cladding, from [27]. Process can be categorized under three sequential categories: **(a)** hydrogen is absorbed by the cladding from the chemical reaction occuring at the outer surface of the cladding with the water, i.e., oxidation via $\text{Zr}+2\text{H}_2\text{O}\rightarrow\text{ZrO}_2+2\text{H}_2$ (*left figure*); **(b)** hydrogen is transported in the cladding via two main diffusion mechanisms in which driving forces are temperature (Soret effect) and concentration gradients (Fick's law) (*middle figure*); and **(c)** hydrogen is either dissolved in the solid solution or precipitates as hydrides whose orientation is heavily dependent on the applied stress (*right figure*).

Instructions   Details of the HNGD modeling in BISON are described in Algorithms 1 through 3. Output parameters from this model are tthe concentration of dissolved hydrogen, C_{ss}, and concentration of hydrogen as hydride, C_{prec}, in addition to the temperature, T, from the coupled heat conduction equation. There are several input parameters—optional parameters with preset default values for the typical Zircaloy cladding—for this model, which are tabulated in Table 2.7. The hydrogen kinetics parameters differentiate for the materials of dissimilar composite clad layers. Some representative experimental values are tabulated in Table 2.8 for hydrogen diffusion kinetics and precipitation/dissolution kinetics of zirconium-hydrides.

Considering the interface of the liner and cladding, the diffusion lengths should be sufficiently small to have accurate predictions between the dissimilar clad layers. This typically requires more refined meshes for the diffusion computations (e.g., hydrogen migration and redistribution modeling in the cladding in our case). To speed up the full-length fuel rod analyses, BISON allows a flexibility to perform a single simulation using two different mesh files at the same time: a coarser mesh for the typical thermo-mechanical fuel rod analysis and a finer mesh for the diffusion calculations. The computational results are performed on the refined mesh for the diffusion calculations and interpolated back to the coarser mesh to complete the typical fuel rod analysis. This can be quite useful in terms of having accurate and faster simulations. This approach has been previously employed by [24] for the spent fuel applications[2] and is useful to investigate cladding failure with a specific hydride distribution—considering the hydride geometry and its distribution within the liner cladding—for full-length fuel rod analyses next year.

Algorithm 1 Algorithm in BISON to compute the hydrogen migration and redistribution.

1: **Input:** $Q^\star$, TSS_{D0}, TSS_{P0}, Q_D, Q_P, and ... (see Table 2.7 for the default values)
2: **Output:** C_{ss}, the concentration of dissolved hydrogen; C_{prec}, the concentration of hydrogen as hydride
3: **procedure**
4:     compute the hydrogen diffusion coefficient using the Arrhenius law: $D = D_0 \exp\left(-E_D/RT\right)$
5:     compute the solubility: $TSS_D = TSS_{D0} \exp\left(-Q_D/RT\right)$
6:     compute the super-solubility: $TSS_P = TSS_{P0} \exp\left(-Q_P/RT\right)$
7:     **if** $C_{ss} < TSS_D$ and $C_{prec} > 0$ **then**
8:         see Algorithm 2: **procedure** DISSOLUTION
9:     **else**
10:         see Algorithm 3: **procedure** NUCLEATION-AND-GROWTH CONTROLLED PRECIPITATION
11:     compute the volume fraction of hydrogen in the α-phase: $\theta = 1 - \Phi/f_{clamp}$ with a user-specified clamping factor of f_{clamp} to limit the maximum allowable volume fraction of hydrides: i.e., $rate* = \theta$
12:     return the concentration of dissolved hydrogen, C_{ss} and hydrogen as hydride, C_{prec}

Algorithm 2 Algorithm in BISON to compute the dissolution for the zirconium hydrides.

1: **procedure** DISSOLUTION
2:     **if** _instantaneous_dissolution **then**
3:         **if** $C_{prec} > (TSS_D - C_{ss})$ **then**
4:             $rate = -(TSS_D - C_{ss})$
5:         **else**
6:             $rate = -C_{prec}$
7:     **else**
8:         compute the kinetic dissolution: $K_D = K_{D0} \exp\left(-E_D/RT\right)$
9:         **if** $C_{prec} > (TSS_D - C_{ss})$ **then**
10:             $rate = \max\left(-K_D\left[TSS_D - C_{ss}\right], -\left[TSS_D - C_{ss}\right]/dt\right)$
11:         **else**
12:             $rate = \max(-K_D C_{prec}, -C_{prec}/dt)$

---

[2]One can find the example BISON input under `bison/examples/spent_fuel/`.

Algorithm 3 Algorithm in BISON to compute the nucleation- and growth-controlled precipitation for the zirconium hydrides.

1: **procedure** NUCLEATION-AND-GROWTH CONTROLLED PRECIPITATION

2:     compute the total hydrogen content $C_{tot} = C_{ss} + C_{prec}$

3:     compute the atomic fraction of hydrogen at the $(\delta/\alpha + \delta)$ boundary: $x_\delta(T) \approx \sum_{i=0}^{3} x_{\delta,i} T^i$ with $\{x_{\delta,i}\}_{i=0}^{3} = \{0.623, -5.73 \times 10^{-5}, 8.48 \times 10^{-8}, -9.93 \times 10^{-11}\}$

4:     compute the atomic fraction of hydride: $x_P = \dfrac{C_{prec}}{\left[M_H\left(\frac{C_{prec}}{M_H} + \frac{1 \times 10^6 - C_{prec}}{M_{Zr}}\right)\right]}$

5:     compute the total atomic fraction of hydrogen: $x_0 = \dfrac{C_{tot}}{\left[M_H\left(\frac{C_{tot}}{M_H} + \frac{1 \times 10^6 - C_{tot}}{M_{Zr}}\right)\right]}$

6:     compute the atomic fraction of hydrogen in the α-phase: $x_\alpha = \dfrac{TSS_D}{\left[M_H\left(\frac{TSS_D}{M_H} + \frac{1 \times 10^6 - TSS_D}{M_{Zr}}\right)\right]}$

7:     compute the volume fraction of α-phase: $f_\alpha = 1 - \frac{x_P}{(x_\delta - x_\alpha)}$

8:     compute the atomic fraction of hydrogen in the α-phase: $v_0 = \frac{(x_0 - x_\alpha)}{(x_\delta - x_\alpha)}$

9:     **if** $C_{ss} > TSS_P$ **then**

10:         compute the hydride formation energy: $E_{th} = \sum_{i=0}^{3} E_{th,i} T^i$ with $\{E_{th,i}\}_{i=0}^{3} = \{-0.5655, 4 \times 10^{-4}, -2 \times 10^{-7}, 3 \times 10^{-10}\}$

11:         compute the nucleation kinetics: $K_N = K_{N0} f_\alpha \chi \exp\left(-E_{th}/RT\right)$ with $\chi = 1 - C_{prec}/1.7 \times 10^4$

12:

13:     **if** growth and $(C_{prec} > 0$ or $rate > 0)$ **then**

14:         compute the growth kinetics: $K_G = \frac{1}{(1/K_{dif} + 1/K_{th})}$ with $K_{dif} = K_{dif0} f_\alpha v_0 \exp\left(-E_G/RT\right)$ and $K_{th} = K_{th0} f_\alpha v_0 \exp\left(-E_{th}/RT\right)$

15:         compute the advancement of transformation: $x = \frac{\delta C_{ss}}{(C_{tot} - TSS_D)}$

16:         **if** $0 < x < 1$ **then**

17:             compute the rate of growth: $\delta C_{ss} = K_G(C_{tot} - TSS_D)p(1-x)([-\ln(1-x)]^{1-1/p})$ with $p = 2.5$

Table 2.7. BISON cladding hydrides action parameters

Symbol	BISON input parameter	Description	Default	Unit
C_{prec}	`hydrogen_as_hydride_ppm`	Concentration of hydrogen as hydride		wt.ppm
C_{ss}	`hydrogen_as_solution_ppm`	Concentration of dissolved hydrogen		wt.ppm
T	`temperature`	Temperature		K
D_0	`diffusivity_frequency_factor`	Frequency factor for Arrhenius hydrogen diffusivity	1.08×10^{-6}	m^2/s
E_D	`diffusivity_activation_energy`	Activation energy for Arrhenius hydrogen diffusivity	44000	J/mol
E_G	`growth_diffusion_kinetic_energy`	Activation energy for Arrhenius reaction-driven growth	86806	J/mol
K_{D0}	`dissolution_kinetic_coef`	Coefficient for Arrhenius dissolution kinetics	1.11×10^3	s^{-1}
K_{dif0}	`growth_reaction_kinetic_coef`	Coefficient for Arrhenius diffusion-driven growth kinetics	1.6×10^{-5}	s^{-1}
K_{th0}	`growth_diffusion_kinetic_coef`	Coefficient for Arrhenius reaction-driven growth kinetics	5.35×10^5	s^{-1}
K_{N0}	`nucleation_kinetic_coef`	Coefficient for Arrhenius nucleation kinetics	2.75×10^{-5}	s^{-1}
$Q^\star$	`heat_of_transport`	Heat of transport for hydrogen in cladding	2.55×10^4	J/mol
Q_D	`solubility_activation_energy`	Activation energy for Arrhenius TSSd	35459	J/mol
Q_P	`super_solubility_activation_energy`	Activation energy for Arrhenius TSSp	25249	J/mol
TSS_{D0}	`solubility_coef`	Frequency factor for Arrhenius TSSd	101999	wt.ppm
TSS_{P0}	`super_solubility_coef`	Frequency factor for Arrhenius TSSp	30853	wt.ppm
f_{clamp}	`hydride_clamp`	Factor limiting the maximum hydride content in a node	1	
	`instantaneous_dissolution` `growth`	Boolean to activate dissolution at equilibrium at all time	False	

Table 2.8. Representative experimental values taken from [25, Table 1–3].

Hydrogen diffusion parameters

Material	$D_0 \times 10^3$ (cm^2/s)	E_D (kJ/mol)	Ref.
Zirconium	7.73	45.3	[29]
	4.15	39.6	[31]
Zircaloy-2	5.84	43.1	[29]
	2.17	35.1	[34]
Zircaloy-4	7.90	44.9	[29]
	0.80	33.2	[37]

Heat of transport

Material	$Q^\star$ (kJ/mol)	Ref.
Zirconium	24.3–25.1	[40]
Zircaloy-4	30.5–31.0	[37]

Precipitation/dissolution kinetics of zirconium-hydrides

Material	Precipitation $TSS_{D0} \times 10^{-3}$ (wt.ppm)	Q_D (kJ/mol)	Dissolution $TSS_{P0} \times 10^{-3}$ (wt.ppm)	Q_P (kJ/mol)	Ref.
Zirconium	49.0208	28.6604	–	–	[30]
	129.3140	36.1079	–	–	[32]
	147.267	35.9824	–	–	[33]
	145.801	35.9406	–	–	[35]
	140.084	36.8192	–	–	[36]
	228.662	39.4133	–	–	[38]
	442.413	44.6014	–	–	[39]
	115.844	35.9406	–	–	[36]
	130.614	36.4426	–	–	[36]
	52.600	28.068	141.000	38.104	[41]
Zircaloy-2	849.655	31.7984	–	–	[34]
	408.399	41.7563	–	–	[38]
	52.600	28.068	128.000	36.540	[42]
	13.320	21.170	108.150	21.170	[43]
	32.700	25.042	143.000	36.686	[44]
Zircaloy-4	681.864	32.3842	–	–	[32]
	40.135	27.336	52.575	32.117	[45]
	66.440	29.630	510.800	45.610	[46]
	31.000	27.678	66.000	35.251	[37]
Zircaloy-2/4	98.7158	34.518	–	–	[36]
	138.7460	34.469	106.4470	35.991	[47]

3. Liner Developments

Liners are used on the interior surface of the cladding in BWRs to mitigate stress corrosion cracking and PCMI failures. The liners are typically made of slightly softer material than the Zircaloy-2 cladding, such as pure zirconium or a low tin content zirconium alloy (e.g., Zr-0.3%Sn).

Prior to this project, the ability to model liners in BISON was limited to using Python mesh scripts in BISON to run the commercial software Cubit/Trelis [48] or using these commercial codes directly. While this possibility remains, it can be cumbersome for users. Therefore, work was completed to add support to the two internal mesh generators within BISON that are typically used within VERA to handle liners and improve ease-of-use. These mesh generators are `SmearedPelletMeshGenerator` and `Layered1DMeshGenerator`. In this chapter, we provide details on how to model liners using the two internal mesh generators as well as with the BISON Python mesh script. The mesh script should be reserved for more complex representations of the fuel rod (e.g., including dishes and chamfers in the fuel). A couple verification problems are also presented to verify that the creation of the internal meshes with liners was properly implemented.

3.1 Internal Meshing Capabilities

Internal meshing capabilities eliminate the need for third-party software to generate the geometries used in fuel performance analyses. By providing capabilities internal to BISON, a user can create the mesh directly in the input file used for the fuel performance simulation. For fuel rod analyses, two geometric representations are used, Layered1D, and 2D-RZ axisymmetric. In BISON, these geometries can be created by the `Layered1DMeshGenerator` and `SmearedPelletMeshGenerator`, respectively. These mesh generators existed in BISON prior to this work, just the capability to include liners in the meshes generated by them was added here.

3.1.1 Layered1DMeshGenerator

In a Layered1D representation of a fuel rod, discrete axial layers are used that each assume axisymmetry. Thermo-mechanics is solved in the radial direction in each layer with out-of-plane effects captured by the use of a generalized plane strain approach. Global fuel rod quantities as rod internal volume, fission gas released, and rod internal pressure are determined by summing the individual contributions from each layer.

To support rapid sensitivity analysis the ability to model liners for 2D-RZ axisymmetric and Layered1D geometries has been added to the internal mesh generators in BISON.

Since the ability to model liners on the interior surface of the cladding was added, a broad range of meshes can be created using the `Layered1DMeshGenerator`.These include, fuel only, cladding only, fuel and cladding, fuel and cladding with a liner, fuel and cladding with a coating, fuel and cladding within a capsule, fuel and cladding with a liner and a coating, fuel and cladding with a liner within a capsule, fuel and cladding with a coating within a capsule, and fuel and cladding with a liner and a coating within a capsule. In all cases, the fuel can either be annular or solid or both. All fuel rod meshes can also contain either or both of upper and lower plenums. Fig. 3.1 presents an example of a Layered1D mesh containing fuel, liner, and cladding. Details of the block names, sidesets, and nodeset conventions created by the mesh generator can be found on the BISON documentation page for the `Layered1DMeshGenerator`.

Figure 3.1. A Layered1D mesh containing fuel and lined cladding.

3.1.2   SmearedPelletMeshGenerator

In a smeared pellet representation of the fuel rod, a 2D-RZ axisymmetric geometry is assumed. The individual fuel pellets are not modeled, and the fuel stack is represented by a rectangle the height of the fuel stack. For many fuel performance calculations, this representation is sufficient. The same combinations of fuel, cladding, and liner as is available for Layered1D are possible, with the exception of including a capsule around the fuel rod. Fig. 3.2 presents an example of smeared pellet mesh containing fuel, liner, and cladding. Details

of the block names, sidesets, and nodeset conventions created by the mesh generator can be found on the BISON documentation page for the `SmearedPelletMeshGenerator` [2].
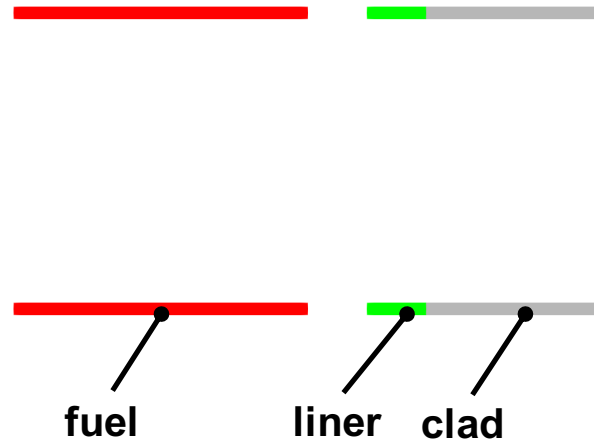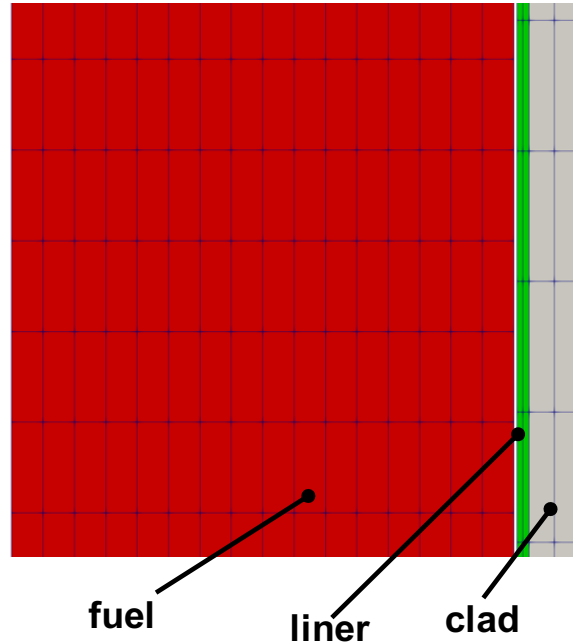

Figure 3.2. A smeared pellet mesh containing a lined cladding.

3.2 BISON Mesh Script

BISON supports an external Python mesh script that interfaces with the CUBIT software [48] that can include liners. The meshing script supports more complex meshes than that of the internal mesh generators such that distinct features of the fuel pellets (e.g., dishes and chamfers) can be captured. The mesh script can also be used to generate three-dimensional representations of the fuel rod. To use the script a user only has to modify the `mesh_script_input.py` file located at `bison/tools/UO2/` within the BISON repository. A portion of the mesh script is shown in the code snippet (see Listing 3.1). To include a liner in your mesh generated by the script the to parameter `clad['with_liner']` needs to be set to `True` and `clad['liner_width']` needs to be specified to a positive non-zero value, as seen in the code snippet. The other parameters are used to define the fuel characteristics and mesh densities. One can see that two different pellet types are defined, one that is solid with dishes and chamfers (`Pellet1`) and an annular pellet with flat end (`Pellet2`). The entire fuel stack is built using the `pellets` to insert the different pellet types in order from the bottom of the fuel stack to the top. In this example, one pellet with `Pellet1` specifications is placed above and below a stack of ten pellets with `Pellet2` specifications. The `angle` parameter defines the number of degrees swept in the azimuthal direction for 3D applications. A value of zero for `angle` results in

a 2D mesh in the x-y plane. Fig. 3.3 presents an example of a discrete mesh containing fuel with dishes and chamfers, a liner, and cladding.
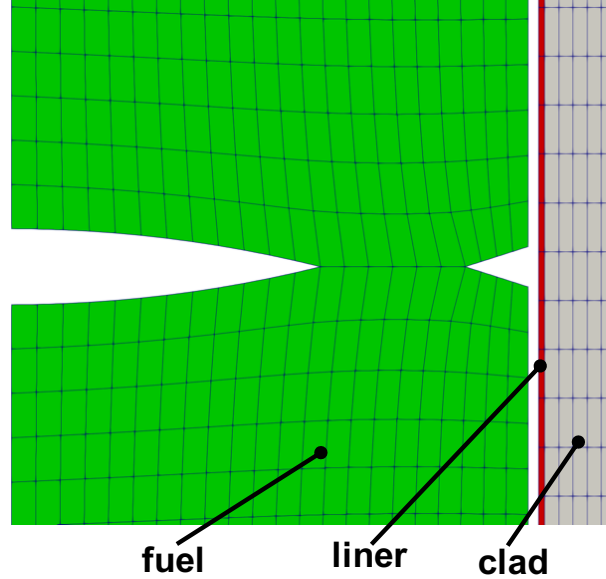
Figure 3.3. Discrete pellet mesh containing dishes and chamfers with a lined cladding.

3.3   Verification

If we consider constant isotropic solid properties, the temperature change across the gap, liner, and cladding can be obtained using the identity of continuous heat flux. This allows to obtain an analytic solution that is more representative of typical fuel rods. An infinitely long fuel rod has a constant thermal conductivity k_f and internal heat generation q'''. It is exposed on its right surface to some constant temperature $T(r_{co}) = T_{co}$ [49]. The temperature jump across the gap, liner, and cladding is:

$$T_f - T_{co} = \frac{q'}{2\pi r_f h_{gap}} + \frac{q'}{2\pi} \left\{ \frac{1}{k_l} \ln \left(\frac{r_{ci}}{r_{li}} \right) + \frac{1}{k_c} \ln \left(\frac{r_{co}}{r_{ci}} \right) \right\}, \tag{3.1a}$$

where T_f is the fuel surface temperature, T_{co} is the cladding outside temperature, k_l is the liner thermal conductivity, and k_c is the cladding thermal conductivity.

The problem in this section focuses on testing the gap heat transfer for an open gap. To simplify the analytic solution, radiative heat transfer is ignored by setting emissivities to zero, and temperature jump distances are set to zero through BISON input. Thus, the gap heat transfer (see Appendix A) reduces to

Listing 3.1. BISON mesh script example.

```
# Pellet Type 1: Active Fuel
# Required parameters
Pellet1= {}
Pellet1[type] = 'discrete'
Pellet1['quantity'] = 10
Pellet1['mesh_density'] = 'coarse'

Pellet1['outer_radius'] = 0.0041
Pellet1['inner_radius'] = 0
Pellet1['height'] = 2*5.93e-3
Pellet1['dish_spherical_radius'] = 1.01542e-2
Pellet1['dish_depth'] = 3e-4
Pellet1['chamfer_width'] = 5.0e-4
Pellet1['chamfer_height'] = 1.6e-4

# Pellet Type 2: Insulators
# Required parameters
Pellet2= {}
Pellet2['type'] = 'discrete'
Pellet2['quantity'] = 1
Pellet2['mesh_density'] = 'coarse'

Pellet2['outer_radius'] = 0.0041
Pellet2['inner_radius'] = 0.0009
Pellet2['height'] = 2*0.106
Pellet2['dish_spherical_radius'] = 0
Pellet2['dish_depth'] = 0
Pellet2['chamfer_width'] = 0
Pellet2['chamfer_height'] = 0

# Pellet Collection
# This list defines the pellets in the fuel stack
# First item is at the bottom of the fuel stack
pellets = [Pellet2, Pellet1, Pellet2]

# Stack options
pellet_stack = {}
pellet_stack['default_parameters'] = False

pellet_stack['interface_merge'] = 'all'   # choose between 'point', 'none' or 'all'
pellet_stack['higher_order'] = False
pellet_stack['angle'] = 0

# Clad: Geometry of the clad
clad = {}
clad['mesh_density'] = 'coarse'
clad['gap_width'] = 8e-5
clad['bot_gap_height'] = 1e-3
clad['clad_thickness'] = 5.6e-4
clad['top_bot_clad_height'] = 2.24e-3
clad['top_gap_height'] = 0.026

clad['with_liner'] = True
clad['liner_width'] = 5.0e-5
```

the fill gas conductance h_g:

$$h_{gap} = h_g = \frac{k_{gas}}{r_f \ln\left(\frac{r_{li}}{r_f}\right)} \tag{3.1b}$$

where k_{gas} is the thermal conductivity of the fill gas and r_{li} is the liner inside radius. The analytic solution for the temperature distribution in the fuel is

$$T(r) = T_f + \frac{q'}{4\pi k_f}\left(1 - \frac{r^2}{r_f^2}\right), \tag{3.1c}$$

where r_f is the fuel radius and k_f is the fuel thermal conductivity.

The problem is run in BISON using three blocks: the fuel domain in $\vec{X} \in [0, 1.0]$, the liner domain in $\vec{X} \in [1.0, 1.05]$, and the clad domain in $\vec{X} \in [1.05, 1.10]$. The domain between the fuel and liner blocks is filled with an inert gas with a predefined gas thermal conductivity. Neumann and Dirichlet boundary conditions are employed: $(dT/dr)_{r=0} = 0$ and $T(r_{co}) = T_{co}$. The steady state heat conduction is considered with the following arbitrarily chosen constants: $k_f = k_c = 10\,\text{W/m/K}$, $k_l = 1\,\text{W/m/K}$, $k_{gas} = 0.1\,\text{W/m/K}$, and $q''' = 400\,\text{W/m}^3$.

Fig. 3.4 shows the exact and computed finite element solutions for two FE types (linear or 1st-order: `EDGE2`; quadratic or 2nd-order: `EDGE3`). The exact and BISON results are in a good agreement, indicating that the new feature 'liner meshing' is correctly coded in BISON and functions as expected.
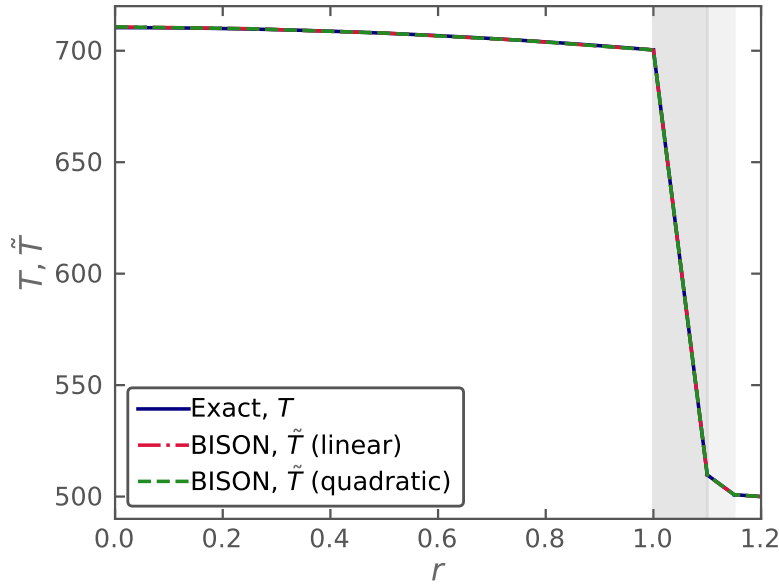

Figure 3.4. Temperature distribution for the verification problem. Exact and FE solutions are obtained using one-dimensional elements.

4. Validation

This chapter focuses on the validation of new modeling options in BISON (from Chapter 2) by comparing code predictions to experimental measurements to determine the applicability of the model to real-world applications. Three rods selected were from the IFA-681.1 test series conducted at the Halden reactor in Norway. The tests investigated here include IFA-681.1 rods 1, 2, and 3. Details of the experimental measurements are described in Section 4.1. Then, BISON simulation settings for the aforementioned experimental data set are outlined in Section 4.2. Lastly, BISON's predictions are compared to the experimental data in Section 4.3, along with the discussion of results.

4.1 Experiment: IFA-681 Rods 1, 2, and 3

The Halden integral test IFA-681 was loaded in the Halden Boiling Water Reactor (HBWR) in January 2005 and operated till February 2012, with a completion of 15 cycles of irradiation. The rig contained two UO_2 fuel rods and four UO_2-Gd_2O_3 rods with varying gadolinia content [0.0, 8.0 wt.%], which were manufactured by Institutt for Energiteknikk (IFE)-Kjeller [50]. An overview on the fuel rod specifictions of the IFA-681 is provided in Table 4.1. In practice, the rod designs were very similar, except for ^{235}U enrichment and Gd concentrations. The experiment was conducted under standard HBWR conditions, with the rig operating at a coolant pressure of approximately 3.5 MPa, and a coolant temperature of approximately $235°C$. Achieved burnup varied was around 31–45 $MWd/kgUO_2$. The aim in the experiment was to evaluate the impact of Gd concentration to the oxide solution on the fuel thermal behavior, dimensional changes, and fission gas release.

The preliminary work was performed by [51] for the initial assessment of the BISON code for the modeling of Gd-doped UO_2 fuel. The analysis in BISON was performed for IFA-681.1 rods 1, 2, and 3 that were solid rods and were enriched to 4.70 wt.%^{235}U for rods 1 and 2, and 2.80 wt.%^{235}U for rod 3. The fuel and cladding specifications are tabulated in Table 4.1. Note that the top 11 pellets are hollow where the thermocouples were located. The integral responses from the experiment were obtained as follows: fuel temperature via a fuel centerline thermocouple, rod internal pressure via pressure transducer, fission gas release (FGR) via the online pressure measurements, and rod power via four neutron detectors install in the rig.

Table 4.1. Fuel rod specifications for IFA-681 [52, 53, 54].

Rod ID	Rod 1	Rod 2	Rod 3
Rod shape	solid	solid	solid
Fuel type	UO_2	UO_2-Gd_2O_3	UO_2-Gd_2O_3
Gd_2O_3 (wt.%)	0.0	2.0	8.0
Enrichment (wt%^{235}U)	4.70	4.70	2.80
Average grain size (μm)	10.9	7.3	8.4
Active stack length (m)	400.4	400.0	400.2
Pellet length (mm)	10.25	9.92	9.97
Pellet OD (mm)	8.19	8.19	8.19
Pellet ID (mm)	0.0/1.8*	0.0/1.8*	0.0/1.8*
Pellet density (%TD)	95.6	96.1	96.0
Cladding material	Zy-4	Zy-4	Zy-4
Cladding ID (mm)	8.36	8.36	8.36
Cladding OD (mm)	9.50	9.50	9.50
Diametral gap (μm)	170	170	170
Free volume (cm^3)	4.6	4.4	4.7
Initial fill gas composition	helium	helium	helium
Fill gas pressure (MPa)	1.0	1.0	1.0

Top 11 pellet only (thermocouple hole)

4.2   BISON Model Settings

Two-dimensional, RZ-problem is setup for the BISON simulations of the IFA-681.1 Rods 1, 2, and 3. The supplementary histories, from Halden data, such linear heat rate (LHR), fast neutron flux, coolant pressure, and coolant inlet temperatures, are provided to BISON. `Fuel Rod Analysis Toolbox` is utilized for the condensation of the data prior to setting the BISON inputs. Radial power factors are computed by [51] at IFE-Halden Reactor Project via the `HELIOS` code [55, 56] to inform BISON analysis. Fig. 4.1 shows the rod average LHR for the aforementioned rods in this study.

Geometry and Mesh

The assumed geometry and mesh are shown in Figure 2 and Figure 3. The fuel pellet stack was modeled as a smeared column with merged insulator pellets (natural UO_2 and Al_2O_3). The analysis in BISON was performed for the three out of six rods, IFA-681 rods 1, 2, and 3. Note that top 11 pellets are hollow where the thermocouple were located. The integral responses from the experiment were obtained as follows: fuel temperature via a fuel centerline thermocouple, rod internal pressure via pressure transducer, FGR via the online pressure measurements, and rod power via four neutron detectors installed in the rig. A two-dimensional axisymmetric geometry was used.

The rod consisted of Al_2O_3 hollow insulation pellets in the upper end of IFA-681 rods 1, 2, and 3, followed by natural UO_2 hollow pellets. The active fuel length consisted of 11 pellets of hollow enriched UO_2 fuel, followed by 28/29 pellets of the solid enriched UO_2 fuel. Similarly, in the lower end of the rods, natural UO_2

Figure 4.1. The average linear heat rate histories for the Halden IFA-681 irradiation.

solid pellets were followed by Al_2O_3 solid insulation pellets.

Material and Behavioral Models

UO_2-Gd_2O_3 fuel   The following material and behavioral models were used for the fuel:

- `ThermalFuel - Toptan` [8]: For temperature and burnup dependent thermal properties.

- `ComputeFiniteStrainElasticStress` and `ComputeIsotropicElasticityTensor`: elastic mechanical behavior

- `UO2VolumetricSwellingEigenstrain`: volumetric expansion due to solid and gaseous swelling

- `UO2RelocationEigenstrain`: relocation strains

- `ComputeThermalExpansionEigenstrain`: thermal expansion with a constant instanteous thermal expansion coefficient

- `Sifgrs`: fission gas release model used with the gaseous swelling model `UO2VolumetricSwellingEigenstrain`

Fuel-to-cladding gap   The following behavioral models of `GapConductanceLWR` were turned on for the gap conductance modeling between the fuel and cladding:

- `TOPTAN`: gap conductance modeling according to [57, 58, 59]

- `ADVANCED`: gas thermal conductivity which takes gas pressure and temperature into account [60]

- `TOPTAN`: temperature jump distance model [57]

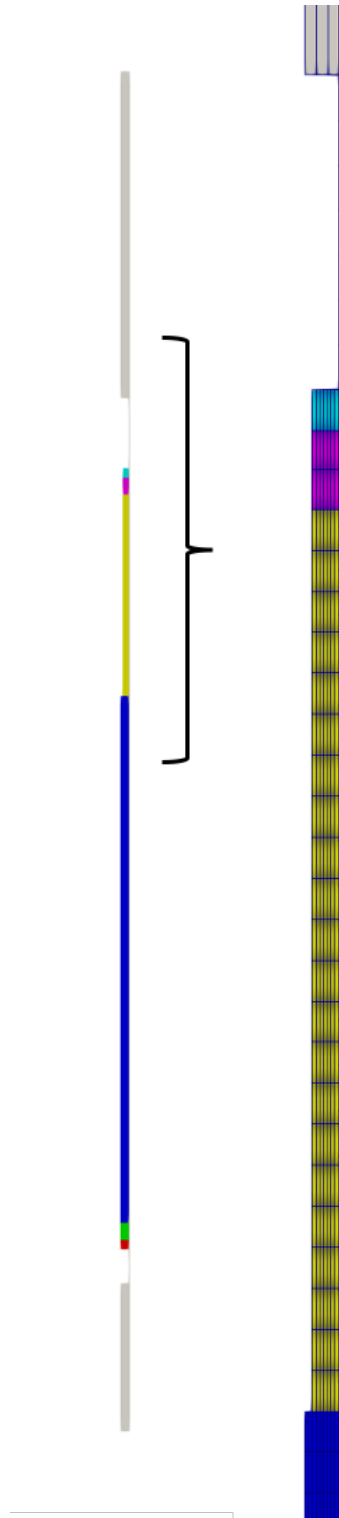- `TOPTAN`: thermal accommodation model [57]

Figure 4.2. A front-view of the IFA-681.1 rod 1 (left) and a close-up view of the IFA-681.1 rod 1, a cut from the top of the fuel rod (right).

Fuel-to-fuel gap   The following behavioral models of `GapConductance` were utilized for the gap conductance modeling of the fuel-to-fuel gap at the thermocouple location considering a constant gas conductivity.

Zircaloy cladding   For the clad material, a constant thermal conductivity of $16\,\text{W/m/K}$ was used, and both thermal (primary and secondary) and irradiation creep were considered using the Limback creep model ([20]). The following material and thermal behavior models were used for the cladding:

- `HeatConductionMaterial`: thermophysical material properties

- `ZryCreepLimbackHoppeUpdate` and `ZryElasticityTensor`: mechanical creep and elastic deformation behavior

- `ZryIrradiationGrowthEigenstrain`: ESCORE model for volumetric swelling due to irradiation exposure

- `ZryThermalExpansionMATPROEigenstrain`: thermal expansion of Zircaloy with the MATPRO model

- `ZryOxidation`: corrosion oxide layer thickness

Natural UO$_2$ material   For the natural UO$_2$ material, a constant thermal conductivity of $3.0\,\text{W/m/K}$ and a constant specific heat capacity of $300\,\text{J/kg/K}$ were used. The following material and thermal behavior models were used for the cladding:

- `HeatConductionMaterial`: Thermophysical material properties

- `ComputeFiniteStrainElasticStress` and `ComputeIsotropicElasticityTensor`: elastic mechanical behavior

- `ComputeThermalExpansionEigenstrain`: thermal expansion with a constant instantaneous thermal expansion coefficient

Al$_2$O$_3$ material   For the Al$_2$O$_3$ material, a constant thermal conductivity of $18.0\,\text{W/m/K}$ and a constant specific heat capacity of $880\,\text{J/kg/K}$ were used. The following material and thermal behavior models were used for the cladding:

- `HeatConductionMaterial`: Thermophysical material properties

- `ComputeFiniteStrainElasticStress` and `ComputeIsotropicElasticityTensor`: elastic mechanical behavior

- `ComputeThermalExpansionEigenstrain`: thermal expansion with a constant instantaneous thermal expansion coefficient

Details and references for all of these models listed above can be found on the linked BISON documentation pages and in the provided inputs.

4.3   Results and Discussion

BISON's predictions are compared to the experimental measurements for each rod in the following sections. A Python postprocessor script was used to extract the centerline temperature at the TC position. It is important to note that the thermocouples and pressure transducers failed, resulting in BISON going to the full time of the average linear heat rate (ALHR) while the experiment doesn't. BISON's temperature predictions are compared to the experimental data for IFA-681.1 Rods 1, 2, and 3 in Fig. 4.3. The new thermal conductivity model, along with the improved gap conductance modeling, results in a good agreement with the measured values for varied gadolinia-doped fuels.
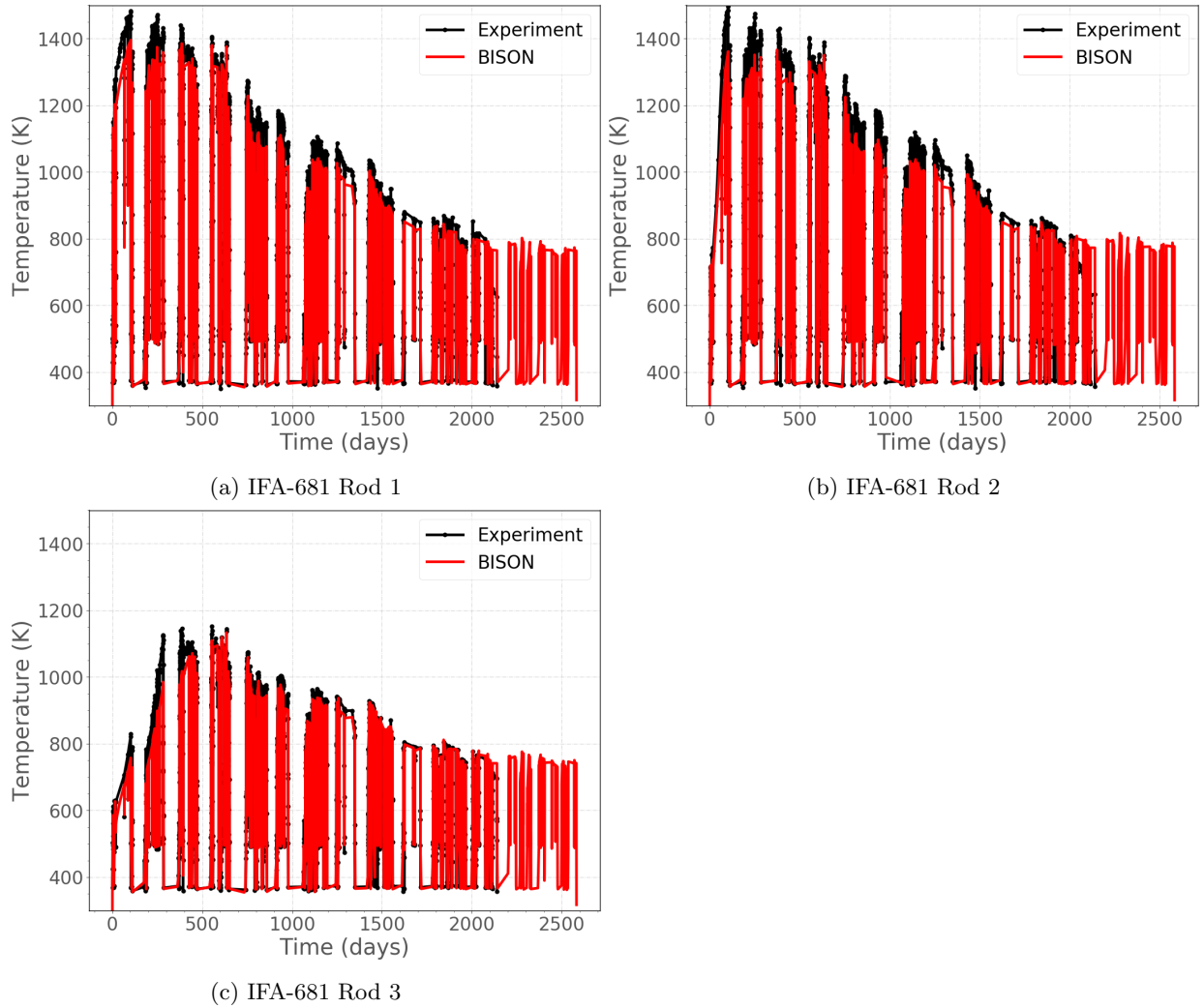

(a) IFA-681 Rod 1

(b) IFA-681 Rod 2

(c) IFA-681 Rod 3

Figure 4.3.   Halden IFA-681.1 fuel temperature histories at TC locations.

5. Concluding Remarks

The BISON fuel performance code has been under development for approximately a decade. Over the years, developments have focused primarily on PWR materials, including potential ATF concepts as well as advanced reactor fuels such as metallic and TRISO fuel particles. The addition of the missing pieces for BWR analyses is required to support the funding opportunity announcement project entitled "Modeling & Analysis of Exelon BWRs with VERA for Eigenvalue and Thermal Limits." The primary focus of this work was to develop the required material models that would aid in predicting cladding failure with a specific hydride distribution, considering the hydride geometry and its distribution within the liner cladding. The BWR modeling capabilities (see Chapter 2) that were made available or revisited in BISON are:

1. UO_2-Gd_2O_3 properties (see Section 2.1): To account for the gadolinia addition to uranium dioxide fuel, two new thermal conductivity models—referred to as `TOPTAN` and `STAICU` for the typical burnup range of interest and the extended burnup applications, respectively—and one specific heat capacity model was implemented (made the default model for the specific heat capacity calculations). In addition to the implementation of new models, existing thermal conductivity models were reviewed again to confirm that the model implementations are correct, and regression tests are added for the models to protect their functionalities for the future code developments. These models are made available in `ThermalFuel` within BISON.

2. Pure zirconium properties (see Section 2.2): Pure zirconium is one of the materials used as a liner material in BWRs. The material property models for pure zirconium is scarce in the literature. The following models were found: thermal conductivity and specific heat capacity as thermal properties that are made available in `ZrThermal` of BISON and thermal expansion as the mechanical property, that is made available in `ZrThermalExpansionEigenstrain` within BISON.

3. Zirconium tin properties (see Section 2.3): Low tin content (<1%) zirconium-tin alloys are another option used for BWR liners. As with pure zirconium, models for low tin content alloys for nuclear applications are scarce. The following model was found in the literature: thermal creep as a mechanical property that was made available in the `ZrSnCreepUpdate` model of BISON.

4. Zircaloy-2 properties (see Section 2.4): Zircaloy-2 is the cladding material of choice in BWRs. Without a specific model for liners, those of Zircaloy-2 are used. We documented the material models available already in BISON for Zircaloy-2 cladding: thermal conductivity and specific heat capacity as thermal properties (`ThermalZry`); and elastic constants (`ZryElasticityTensor`), thermal expansion

(`ZryThermalExpansionEigenstrain`), thermal and irradiation creep (`ZryCreepLOCAErbacherLimbackHoppeUpdate`), and irradiation growth (`ZryIrradiationGrowthEigenstrain`) as mechanical properties.

5. Hydrogen migration/redistribution behavior model (see Section 2.5): BISON's existing model for the hydrogen migration and redistribution in the cladding was documented. Details of the up-to-date model (available) in the code were provided. Instructions were provided for the users on how to use this modeling option for a liner cladding geometry, along with some representative experimental values of the hydrogen diffusion and precipitation-dissolution kinetics of zirconium hydrides for pure zirconium, Zircaloy-2, and Zircaloy-4. A detailed analysis on the prediction of cladding failure with a specific hydride distribution is a primary focus of the next year's milestones.

Another task of this milestone was to develop liner meshing capabilities in BISON for BWR applications (see Chapter 3) to support ease-of-use and industry adoption of the code. Liners are used on the interior surface of the cladding in BWRs to mitigate stress corrosion cracking and PCMI failures. One can use external meshing tools such as Cubit/Trelis to create any type of geometry. To provide ease-of-use and to handle the mesh generation internally within BISON, the ability to handle liners was added to two exiting internal meshing capabilities:

1. `Layered1DMeshGenerator` models the fuel rod as an axial stack of one-dimensional radial analyses assuming azimuthal symmetry. Global quantities are computed by summing the individual contributions from the different layers. Meshes can include fuel, cladding, liner, and a capsule, or any combination of them.

2. `SmearedPelletMeshGenerator` models the fuel rod in a 2D-RZ axisymmetric representation with the fuel assumed to be a smeared column (i.e., right cylinder without dishes and chamfers). Meshes can include fuel, cladding, liner, and a capsule, or any combination of them.

3. Verification of the internal meshing capabilities was accomplished by simulating a simplistic thermal problem and demonstrating proper convergence behavior. This ensures that the internal meshing capabilities are generating properly connected meshes.

As a best practice of software quality assurance (SQA), all of these modeling features are documented, integrated into BISON, and run periodically to ensure that code capabilities are not lost as changes are made. This is achieved using regression tests that also serve as examples for the users how to use each modeling option in the code.

Validation is the comparison of model predictions to experimental measurements to determine the accuracy at which the simulations predict reality. Here, validation focused on the the Gd-bearing UO_2 model developments, in particular, the new thermal conductivity models. Three rods from the IFA-681 series irradiated at the Halden reactory in Norway were analyzed. The rods were a non-doped UO_2, a 2 wt.% Gd_2O_3 and a 8 wt.% Gd_2O_3 rod. Thermocouple temperature comparisons were in a very good agreement (see Chapter 4).

In addition to the aforementioned BWR material developments described in detail in this report, one journal article described BISON models for gadolinia-doped UO_2, including verification and validation (see Chapter 6).

This work establishes a strong base for BISON's BWR modeling capabilities for Gd-doped UO_2 fuels with lined cladding, which is to be expanded next year. In the future, this work will be expanded to include hydrogen and hydride embrittlement and its impact on failure predictions. Additional applications will be performed in BISON for BWR fuel behavior during normal operations (including control blade sequence exchanges involving down power and return to power maneuvers) and anticipated transients such as a reactivity insertion accident (RIA) driven by a control rod drop accident to examine whether PCMI is a potential failure mechanism and to identify what the failure limits should be for BWR cladding.

The milestones to be completed in `FY2021` can be listed as:

1. to perform and document sensitivity analyses for BWR fuel (due `4/30/2021`) and

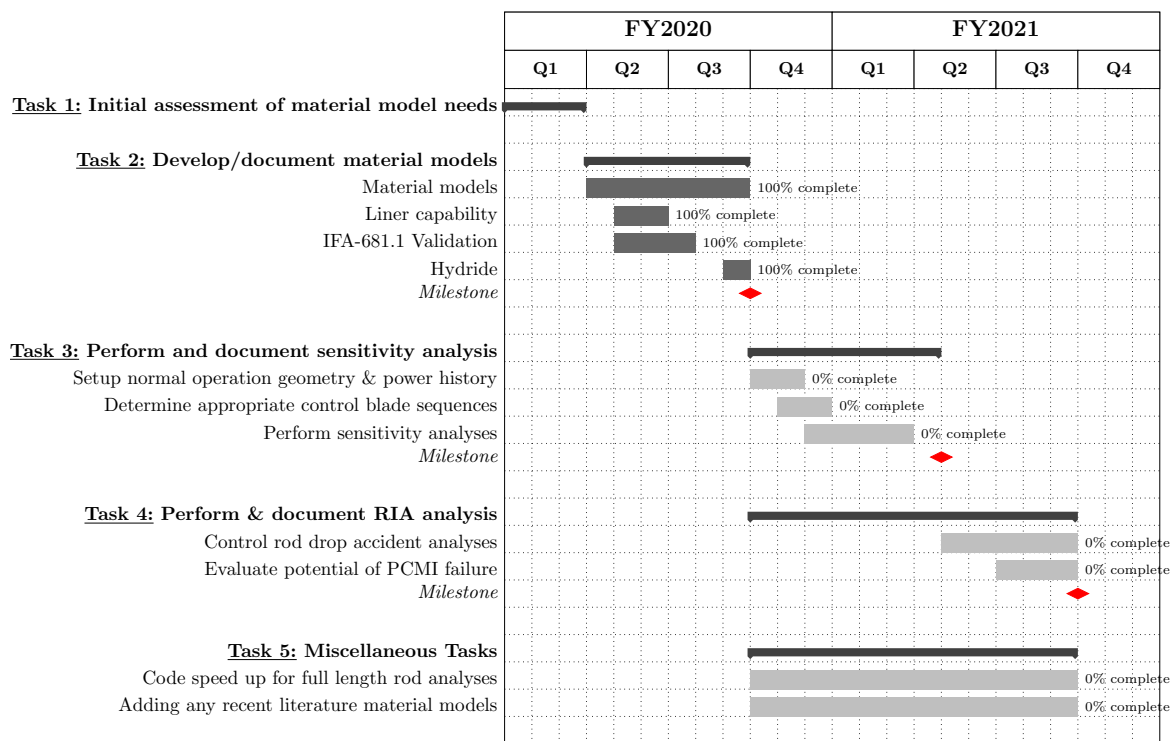2. to perform and document RIA analysis for BWR fuel (due `9/30/2021`).

Figure 5.1. Gantt diagram for 2020–2021 fiscal years

6. Publications

In regards to BWR capabilities in BISON, one journal article is under revision that illustrates the model development including validation. Highlights of the publication(s) are briefly provided as follows:

1. A. Toptan, G. Pastore, J.D. Hales, S. R. Novascone, R. L. Williamson, "Engineering-scale Modeling of Thermal Conductivity in BISON for UO_2 and Gd-bearing UO_2 Fuels," Journal of Nuclear Materials, 2020 (*submitted, under review*).

   Highlights:

   - An extensive literature survey for the development of an engineering-scale thermal conductivity model for uranium dioxide, including gadolinia-doping.

   - Identified associated uncertainties in the models along with underlying assumptions.

   - To assess the performance of thermal conductivity models, including the newly developed model in this study and the conventional thermal conductivity models commonly used in nuclear applications, the models are compared to each other (see Fig. 6.1) and to experimental data.

   - A new postulated engineering-scale modeling strategy to allow flexibility in updating the thermal conductivity component for extended burnups.

Figure 6.1. Comparisons of model predictive envelopes for the stoichiometric UO$_2$ thermal conductivity in **(a)** the burnup range varied from 0 to 60 MWd/kgU and **(b)** the gadolinia concentration varied from 0 to 10 wt %. The predictions from the proposed model (see `TOPTAN` model in Property 2.1; *referred to as Eq.(6) on each plot*) are plotted in each plot for ease of comparison with the other thermal conductivity models. Note that addition of either burnup or gadolinia degrades the thermal conductivity; therefore, the upper bound represents the non-doped fuel at zero burnup, and the lower bound represents the irradiated and Gd-doped fuel.

Bibliography

[1]   R. L. Williamson et al. "Multidimensional multiphysics simulation of nuclear fuel behavior". In: *Journal of Nuclear Materials* 423.1–3 (2012), pp. 149–163. DOI: `10.1016/j.jnucmat.2012.01.012`.

[2]   J. D. Hales et al. *BISON Theory Manual The Equations Behind Nuclear Fuel Analysis*. Idaho National Laboratory. Idaho Falls, Idaho, 2014.

[3]   R. L. Williamson, J. D. Hales, et al. "BISON: A flexible code for advanced simulation of the performance of multiple nuclear fuel forms". In: *Nuclear Technology* (2020). *submitted*.

[4]   D. Gaston et al. "MOOSE: A parallel computational framework for coupled systems of nonlinear equations". In: *Nuclear Engineering and Design* 239.10 (2009), pp. 1768–1778. DOI: `10.1016/j.nucengdes.2009.05.021`.

[5]   C.J. Permann et al. "MOOSE: Enabling massively parallel multiphysics simulation". In: *SoftwareX* 11 (2020), p. 100430. DOI: `10.1016/j.softx.2020.100430`.

[6]   J. D. Hales et al. "Multidimensional multiphysics simulation of TRISO particle fuel". In: *Journal of Nuclear Materials* 443 (2013), pp. 531–543. DOI: `10.1016/j.jnucmat.2013.07.070`.

[7]   J. D. Hales et al. *BISON TRISO Modeling Advancements and Validation to AGR-1 Data*. PEMP Notable Outcome 1.1.C Completion Report INL/EXT-20-00297. Idaho National Laboratory, July 2020.

[8]   A. Toptan et al. "Engineering-scale modeling of thermal conductivity in BISON for UO_2 and Gd bearing UO_2 fuels". In: *Journal of Nuclear Materials* (2020). (*submitted*).

[9]   J. C. Maxwell. *Treatise on Electricity and Magnetism*. Oxford University Press Oxford, 1873/1904.

[10]   G. Ondracek and B. Schultz. "The porosity dependence of the thermal conductivity for nuclear fuels". In: *Journal of Nuclear Materials* 46.3 (1973), pp. 253–258. DOI: `10.1016/0022-3115(73)90039-1`.

[11]   C. Ronchi et al. "Effect of burn-up on the thermal conductivity of uranium dioxide up to 100.000 MWd t^{-1}". In: *Journal of Nuclear Materials* 327.1 (Apr. 2004), pp. 58–76. DOI: `10.1016/j.jnucmat.2004.01.018`.

[12]   D. Staicu et al. "Effect of burn-up on the thermal conductivity of uranium–gadolinium dioxide up to 100 GWd/tHM". In: *Journal of Nuclear Materials* 453 (2014), pp. 259–268. DOI: `10.1016/j.jnucmat.2014.07.006`.

[13]   D. Staicu. "2.17 - Thermal Properties of Irradiated UO$_2$ and MOX". In: *Comprehensive Nuclear Materials* 2 (2012), pp. 439–464. DOI: 10.1016/B978-0-08-056033-5.00038-0.

[14]   D.D. Lanning, C.E. Beyer, and K.J. Geelhood. *FRAPCON-3 Updates, including Mixed-Oxide fuel properties.* Tech. rep. NUREG/CR-6534, Vol.4; PNNL-11513. Richland, WA 99532: Pacific Northwest National Laboratory, 2005. URL: https://www.nrc.gov/docs/ML0514/ML051440720.pdf.

[15]   A. Marion. *Letter dated June 13, 2016 to HN Berkow (USNRC/NRR).* Tech. rep. Nuclear Energy Institute (NEI), 2006. URL: https://www.nrc.gov/docs/ML0616/ML061650107.pdf.

[16]   W. F. Lyon. *Summary report: Gd thermal conductivity model updates.* Tech. rep. ANA-P1400138-TN03 Rev. 2. Anatech Corp., 2015.

[17]   W.J. Luscher, K.J. Geelhood, and I.E. Porter. *Material Property Correlations: Comparisons between FRAPCON-4.0, FRAPTRAN-2.0, and MATPRO.* Tech. rep. PNNL-19417 Rev. 2. Pacific Northwest National Laboratory, Sept. 2015.

[18]   J.K. Fink and L. Leibowitz. "Thermal conductivity of zirconium". In: *Journal of Nuclear Materials* 226.1–2 (1995), pp. 44–50. DOI: 10.1016/0022-3115(95)00110-7.

[19]   S.K. Jha, S. Dixit, and D. Srivastava. "Study of Thermomechanical Behavior of Zirconium-0.3 Tin Alloy". In: *Journal of Materials Engineering and Performance* 28 (2019), pp. 5127–5137. DOI: 10.1007/s11665-019-04204-x.

[20]   M. Limbäck and T. Andersson. "A Model for Analysis of the Effect of Final Annealing on the In- and Out-of-Reactor Creep Behavior of Zircaloy Cladding". In: *Zirconium in the Nuclear Industry: Eleventh International Symposium.* ASTM STP 1295. 1996, pp. 448–468.

[21]   F. J. Erbacher et al. "Burst criterion of Zircaloy fuel claddings in a loss-of-coolant accident". In: *Zirconium in the Nuclear Industry, Fifth Conference, ASTM STP 754, D.G. Franklin Ed.* American Society for Testing and Materials. 1982, pp. 271–283.

[22]   Q. Auzoux et al. "Hydride reorientation and its impact on ambient temperature mechanical properties of high burn-up irradiated and unirradiated recrystallized Zircaloy-2 nuclear fuel cladding with an inner liner". In: *Journal of Nuclear Materials* 494 (2017), pp. 114–126. DOI: 10.1016/j.jnucmat.2017.07.022.

[23]   E. Nagase and T. Fuketa. "Influence of Hydride Re-orientation on BWR Cladding Rupture under Accidental Conditions". In: *Journal of Nuclear Science and Technology* 41.12 (2004), pp. 1211–1217. DOI: 10.1080/18811248.2004.9726350.

[24]   D. S. Stafford. "Multidimensional simulations of hydrides during fuel rod lifecycle". In: *Journal of Nuclear Materials* 466 (2015), pp. 362–372. DOI: 10.1016/j.jnucmat.2015.06.037.

[25]   Z. Aly et al. "Variance-based sensitivity analysis applied to hydrogen migration and redistribution model in Bison. Part I: Simulation of historical experiments". In: *Journal of Nuclear Materials* 524 (2019), pp. 90–100. DOI: 10.1016/j.jnucmat.2019.06.035.

[26] Z. Aly et al. "Variance-based sensitivity analysis applied to the hydrogen migration and redistribution model in Bison. Part II: Uncertainty quantification and optimization". In: *Journal of Nuclear Materials* 523 (2019), pp. 478–489. DOI: 10.1016/j.jnucmat.2019.06.023.

[27] Florian Passelaigue. *Hydride Nucleation - Growth - Dissolution Model: Implementation in BISON.* 2020. URL: https://etda.libraries.psu.edu/catalog/17572fpp8.

[28] G. Pastore et al. *Hydrogen Migration and Redistribution in BISON.* Tech. rep. INL/EXT-20-00214. Idaho National Lab.(INL), Apr. 2020.

[29] J. Kearns. "Diffusion coefficient of hydrogen in alpha zirconium, Zircaloy-2 and Zircaloy-4". In: *Journal of Nuclear Materials* 43.3 (1972), pp. 330–338. DOI: 10.1016/0022-3115(72)90065-7.

[30] C.M. Schwartz and M.W. Mallett. In: *Trans. Amer. Soc. Metals.* Vol. 46. 1954, pp. 640–654.

[31] M. Someno and N.K. Gakkaishi. "Solubility and diffusion of hydrogen in zirconium". In: *J. Japan Inst. Metals* 24.4 (1960). (in Japanese), pp. 249–253. URL: https://www.jim.or.jp/journal/j/24/04/249-253.html.

[32] E.A. Gulbransen and K.F. Andrew. "Solubility and Decomposition Pressures of Hydrogen in Alpha-Zirconium". In: *Trans. AIME 203.* Vol. 7. 1955, pp. 136–144. DOI: 10.1007/BF03377469.

[33] M.W. Mallett and W.M. Albrecht. "Low-Pressure Solubility and Diffusion of Hydrogen in Zirconium". In: *Journal of The Electrochemical Society* 104.3 (1957). URL: https://iopscience.iop.org/article/10.1149/1.2428522.

[34] A. Sawatzky. "The diffusion and solubility of hydrogen in the alpha phase of zircaloy-2". In: *Journal of Nuclear Materials* 2.1 (1960), pp. 62–68. DOI: 10.1016/0022-3115(60)90025-8.

[35] T.B. Douglas. "The Zirconium-Hydrogen System: Some Thermodynamic Properties from a Heat Content Study". In: *Journal of the American Chemical Society* 80.19 (1958), pp. 5040–5046. DOI: 10.1021/ja01552a010.

[36] J.J. Kearns. "Terminal solubility and partitioning of hydrogen in the alpha phase of zirconium, Zircaloy-2 and Zircaloy-4". In: *Journal of Nuclear Materials* 22.3 (1967), pp. 292–303. DOI: 10.1016/0022-3115(67)90047-5.

[37] B. Kammenzind et al. "Hydrogen pickup and redistribution in alpha-annealed Zircaloy-4". In: *E.R. Bradley, G.P. Sabol (Eds.), Zirconium in the Nuclear Industry: Eleventh International Symposium, ASTM STP 1295.* 1996, pp. 338–370.

[38] G.Östberg. "Determination of hydride solubility in alpha phase zirconium, zircaloy-2 and zircaloy-4". In: *Journal of Nuclear Materials* 5.2 (1962), pp. 208–215. DOI: 10.1016/0022-3115(62)90101-0.

[39] W.H. Erickson and D. Hardie. "The influence of alloying elements on the thermal solubility of hydrogen in α-zirconium". In: *Journal of Nuclear Materials* 13.2 (1964), pp. 254–262.

[40] A. Sawatzky. "The heat of transport of hydrogen in zirconium alloys". In: *Journal of Nuclear Materials* 9.3 (1963), p. 364. DOI: 10.1016/0022-3115(63)90154-5.

[41] K. Une and S. Ishimoto. "Terminal Solid Solubility of Hydrogen in Unalloyed Zirconium by Differential Scanning Calorimetry". In: *Journal of Nuclear Science and Technology* 41.9 (2004), pp. 949–952. DOI: `10.1080/18811248.2004.9715569`.

[42] K. Une and S. Ishimoto. "Dissolution and precipitation behavior of hydrides in Zircaloy-2 and high Fe Zircaloy". In: *Journal of Nuclear Materials* 322.1 (2003), pp. 66–72. DOI: `10.1016/S0022-3115(03)00320-9`.

[43] K.B. Colas. *Fundamental Experiments on Hydride Reorientation in Zircaloy*. 2012.

[44] K. Une et al. "The terminal solid solubility of hydrogen in irradiated Zircaloy-2 and microscopic modeling of hydride behavior". In: *Journal of Nuclear Materials* 389.1 (2009), pp. 127–136. DOI: `10.1016/j.jnucmat.2009.01.017`.

[45] R. Tang and X. Yang. "Dissolution and precipitation behaviors of hydrides in N18, Zry-4 and M5 alloys". In: *Int. J. Hydrogen Energy* 34.17 (2009), pp. 7269–7274. DOI: `10.1016/j.ijhydene.2009.07.018`.

[46] O. Zanellato, M. Preuss, J.-Y. Buffiere, et al. "Synchrotron diffraction study of dissolution and precipitation kinetics of hydrides in zircaloy-4". In: *Journal of Nuclear Materials* 420.1–3 (2012), pp. 537–547. DOI: `10.1016/j.jnucmat.2011.11.009`.

[47] A. McMinn, E. Darby, and J. Schofield. "The terminal solid solubility of hydrogen in zirconium alloys". In: *Zirconium in the Nuclear Industry: 12th International Symposium*. 2000, pp. 173–195.

[48] M. Skroch et al. *CUBIT: Geometry and Mesh Generation Toolkit, 15.5 User Documentation*. Tech. rep. SAND2019-3478W. Sandia National Laboratories, 2019.

[49] A. Toptan et al. *FY20 Verification of BISON Using Analytic and Manufactured Solutions*. Tech. rep. CASL-U-2020-1939-000; SAND2020-3887R. Sandia National Lab.(SNL), 2020. DOI: `10.2172/1614683`.

[50] J. D. Hales et al. "Solving Nonlinear Solid Mechanics Problems with the Jacobian-Free Newton Krylov Method". In: *Computer Modeling in Engineering & Sciences* 84.2 (2012), pp. 123–154. DOI: `10.3970/cmes.2012.084.123`.

[51] G. Pastore et al. "Modelling of the Galolinium Fuel Test IFA-681 using the BISON code". In:

[52] F. Khattout. *The Gadolinia Fuel Test IFA-681: Overview of In-Pile Measurements From Beginning of Irradiation to Unloading*. Tech. rep. HWR-1038. OECD Halden Reactor Project, 2013.

[53] V. Colombier et al. *Comparative Study of the Gadolinia Experiments IFA-515.10, IFA-636, IFA-681.1, and IFA-676.1*. Tech. rep. HWR-924. OECD Halden Reactor Project, 2010.

[54] Institutt for Energiteknikk OECD Halden Reactor Project. *Data Sheet / IFA-681.1, Technical Note*. 2005.

[55] R. J. J. Stammler (Ed.) *HELIOS documentation*. Tech. rep. Norway: FMS Fuel Management System, Studsvik Scandpower, 2000.

[56] J.-C. Kim. *Physics calculations for IFA-681.1*. Tech. rep. CP note 03-51. OECD Halden Reactor Project, 2003.

[57] A. Toptan, D. J. Kropaczek, and M. N. Avramova. "Gap conductance modeling I: Theoretical considerations for single- and multi-component gases in curvilinear coordinates". In: *Nuclear Eng Design* 353 (2019). DOI: `10.1016/j.nucengdes.2019.110283`.

[58] A. Toptan, D. J. Kropaczek, and M. N. Avramova. "Gap conductance modeling II: Optimized model for UO_2-Zircaloy interfaces". In: *Nuclear Eng Design* 355 (2019). DOI: `10.1016/j.nucengdes.2019.110289`.

[59] A. Toptan et al. "Modeling of gap conductance for LWR fuel rods applied in the BISON code". In: *Journal of Nuclear Science and Technology* 57.8 (2020), pp. 963–974. DOI: `10.1080/00223131.2020.1740808`.

[60] A. Toptan, D. J. Kropaczek, and M. N. Avramova. "On the Validity of the Dilute Gas Assumption for Gap Conductance Calculations in Nuclear Fuel Performance Codes". In: *Nuclear Eng Design* 350 (2019), pp. 1–8. DOI: `10.1016/j.nucengdes.2019.04.042`.

[61] A. Toptan. "A Novel Approach to Improve Transient Fuel Performance Modeling in Multi-Physics Calculations". PhD thesis. North Carolina State University, 2019. URL: `https://repository.lib.ncsu.edu/handle/1840.20/36352`.

A. Gap Conductance: Thermal Aspects

The temperature jump across the gap in BISON is computed as a summation of heat transfers: fill gas conductance h_g, contact conductance h_c, and radiative conductance h_r [2, 60, 57, 58, 59, 61]:

$$h_{gap} = h_g + h_c + h_r, \tag{A.1a}$$

where

$$h_g = \begin{cases} \dfrac{k_{gas}}{d + g_1 + g_2} & \text{plane} \\[2ex] \dfrac{k_{gas}}{r_1 \left(\ln\left(\frac{r_2}{r_1} \right) + \frac{g_1}{r_1} + \frac{g_2}{r_2} \right)} & \text{cylinder} \\[2ex] \dfrac{k_{gas}}{r_1^2 \left(\left[\frac{1}{r_1} - \frac{1}{r_2} \right] + \frac{g_1}{r_1^2} + \frac{g_2}{r_2^2} \right)} & \text{sphere} \end{cases}, \tag{A.1b}$$

$$h_c = C \frac{\Lambda}{r_a} \left(\frac{W}{H} \right), \tag{A.1c}$$

$$h_r = \frac{\sigma_{SB}(T_1^2 + T_2^2)(T_1 + T_2)}{\dfrac{1}{\varepsilon_1} + \left(\dfrac{1}{\varepsilon_2} - 1 \right)}. \tag{A.1d}$$

where k_{gas} is the fill gas thermal conductivity, d is the gap distance, g_i is the temperature jump distance, Λ is the harmonic mean of thermal conductivities of the surrounding solids, r_a is the contact radius that is defined as a function of the surface roughness, W is the load on the contact interface, H is the Meyer's hardness of the softer material, σ_{SB} is the Stefan-Boltzmann constant, T_i is temperature, ε_i is the emissivity, and r_i is the radius for the solid bodies $i = 1, 2$ ($r_1 < r_2$).